Description of the LASSO Alpha 1 Release

William I. Gustafson, Jr.[1] (PI), Andrew M. Vogelmann[2] (Co-PI), Xiaoping Cheng[3], Satoshi Endo[2], Bhargavi Krishna[4], Zhijin Li[3,5], Tami Toto[2], and Heng Xiao[1]

[1]Atmospheric Sciences & Global Change Division
Pacific Northwest National Laboratory

[2]Environmental & Climate Sciences Department
Brookhaven National Laboratory

[3]Joint Institute for Regional Earth System Science & Engineering
University of California, Los Angeles

[4]Climate Change Science Institute
Oak Ridge National Laboratory

[5]Ocean Circulation and Air Sea Interaction Group
Jet Propulsion Laboratory

July 2016

Alpha 1 Release Webpage:
http://www.arm.gov/science/themes/lasso/releases/

Alpha 1 Dataset DOI: 10.5439/1256454

Table of contents

1 Introduction

1.1 The LASSO Project

The Department of Energy (DOE) Atmospheric Radiation Measurement (ARM) Climate Research Facility began a pilot project in May 2015 to design a routine, high-resolution modeling capability to complement ARM's extensive suite of measurements. This modeling capability has been named the Large-Eddy Simulation (LES) ARM Symbiotic Simulation and Observation (LASSO) project.

The availability of LES simulations with concurrent observations will serve many purposes. LES helps bridge the scale gap between DOE ARM observations and models, and the use of routine LES adds value to observations. It provides a self-consistent representation of the atmosphere and a dynamical context for the observations. Further, it elucidates unobservable processes and properties. LASSO will generate a simulation library for researchers that enables statistical approaches beyond a single-case mentality. It will also provide tools necessary for modelers to reproduce the LES and conduct their own sensitivity experiments.

Many different uses are envisioned for the combined LASSO LES and observational library. For an observationalist, LASSO can help inform instrument remote sensing retrievals, conduct Observation System Simulation Experiments (OSSEs), and test implications of radar scan strategies or flight paths. For a theoretician, LASSO will help calculate estimates of fluxes and co-variability of values, and test relationships without having to run the model yourself. For a modeler, LASSO will help one know ahead of time which days have good forcing, have co-registered observations at high-resolution scales, and have simulation inputs and corresponding outputs to test parameterizations. Further details on the overall LASSO project are available at http://www.arm.gov/science/themes/lasso.

1.2 The LASSO Alpha 1 Release

This Alpha 1 release is the first dissemination of simulations and analysis tools from LASSO focusing on five shallow convection cases conducted at the ARM Southern Great Plains (SGP) Climate Research Facility. The release occurs roughly one year into the pilot project lifecycle and is in the form of an ARM Evaluation Product. The complete set of data products and tools can be accessed via http://www.arm.gov/science/themes/lasso/releases/. This web page serves as a high-level interface to the data files, collectively called data bundles, that consist of LES input and outputs, ARM observations co-registered on the model grid, model diagnostics and skill scores, and quicklooks of various fields. An interface is provided through a web browsing tool, called the LASSO Bundle Browser, for users to find simulations of interest through examination of the LES performance relative to select ARM observations.

This release contains a battery of 192 simulations and model-observation comparisons for different LES models, large-scale forcings, model configurations, and preliminary observational products that the LASSO team are using to assess workflow options for use in operations. Simulations from both the System for Atmospheric Modeling (SAM) and the Weather Research and Forecasting (WRF) model are available. They are combined with a range of forcings under consideration for use in LASSO combined with the sensitivity of model simulations to model selection and physics options. Many of the simulations are directly comparable, *e.g.*, they use the same model configuration and only differ in the forcing or initial conditions used to drive the model. Other simulations differ in the particular choice of microphysics. The release also serves as an initial introduction to the skill scores being designed for model evaluation. Preliminary effort has gone into designing the Bundle Browser interface to help users find simulations of relevance for their needs, which is a tool based on the Cassandra NoSQL database methodology.

The simulations within this release represent the typical behavior to be expected from LES using best-practice configurations and are valid for use in various research applications. However, as made evident by the comparisons to observations, there is a range of model behavior so we encourage users to contact the LASSO team to ensure the details of the simulations are understood and that they are used appropriately for their application.

A key objective for the Alpha 1 release is to solicit feedback from the community. Efforts to improve the model configuration, forcings, and analysis tools are ongoing and will evolve particularly over the coming year based on user

feedback and continued effort. We encourage users to explore the available simulations and tools and to share their experience and ideas for improvement with the LASSO team (William.Gustafson@pnnl.gov, vogelmann@bnl.gov).

1.3 Highlighted Links

The Alpha 1 release consists of several components available at different locations due to the format of the ARM infrastructure. However, the components are intended to be viewed as a single entitiy packaged as DOI:10.5439/1256454. Links to the different components are listed below.

Overview web page: http://www.arm.gov/science/themes/lasso/releases/
Documentation files: http://iop.archive.arm.gov/arm-iop/0eval-data/gustafson/lasso-alpha1/docs/
Data bundle files: http://iop.archive.arm.gov/arm-iop/0eval-data/gustafson/lasso-alpha1/
Bundle Browser: http://archive.arm.gov/lassobrowser

1.4 Proper Acknowledgement when Using the Alpha 1 Release

At the time of the release, the Alpha 1 simulations and tools are not yet documented in a peer reviewed article. We therefore request that users publishing with the Alpha 1 products consider including appropriate LASSO team members as co-authors. Contact the LASSO principal investigator (PI) (william.gustafson@pnnl.gov) for specifics regarding the different team member contributions.

The LASSO Alpha 1 data and methodologies should be cited as:

> Atmospheric Radiation Measurement (ARM) Climate Research Facility. LASSO Alpha 1 Data Bundles. http://dx.doi.org/10.5439/1256454.

At a minimum, ARM requests the following acknowledgement:

> LASSO data were used from the U.S. Department of Energy's Atmospheric Radiation Measurement (ARM) Climate Research Facility.

2 Modeling Details

2.1 LES Model Configuration

Two models are being evaluated for ongoing use in LASSO. One is the SAM model [Khairoutdinov and Randall, 2003] version 6.10.6 and the other is the WRF model version 3.7 [Skamarock et al., 2008] version 3.7 with additional components developed for the DOE FASTER project [Endo et al., 2015]. The two models have been configured as similarly as possible to enable pairs of simulations to be compared for a given set of forcing and domain configurations. The WRF-FASTER modification to WRF includes LES-specific output, such as domain averaged profiles that are time averaged between output times based on a specified sampling frequency, making it similar to how SAM handles output. Small changes have been made to the SAM model to make its handling of initial conditions more consistent to WRF-FASTER.

Physics between the two models are generally similar. Most simulations in this release use Morrison microphysics [Morrison et al., 2005; Morrison et al., 2009], as this is available in both SAM and WRF. An additional set of simulations have been done using the Thompson scheme [Thompson et al., 2004; Thompson et al., 2008] with WRF to evaluate sensitivity to the microphysics choice. The resulting shallow clouds are similar between the two options. However, Morrison generates more cirrus than Thompson. The version of Morrison in WRF-FASTER is slightly older than in SAM, but the two behave similarly. The shortwave and longwave RRTMG radiation schemes are used for both models [Clough et al., 2005; Iacono et al., 2008; Mlawer et al., 1997]. The subgrid-scale scheme is based on the 1.5 order TKE approach [Deardorff, 1980] for both models.

The domain configurations for the Alpha 1 release use 100 m grid spacing. Most simulations have been run using a domain that is 14.4 km across, with some larger 25 km domains also available. Several variations for the vertical levels and spacing have been tested, with most of the released simulations using 226 levels that extend

from the surface to 14.7 km. Vertical grid spacing is 30 m up to 5 km and then stretches to 300 m near the model top. We recognize that, while these all-purpose configurations are sufficient for testing the model forcings and various scientific applications, higher resolutions or larger domains may be desirable for some applications. To assist those researchers, we make the input forcings, assessments of their quality, and model evaluation data available so that these simulations may serve as a starting point for their own simulations configured and tailored to their needs (see the Data Bundles Section).

Other details for the model setups can be found in the config directories associated with each model simulation. The model codes are mostly out-of-the-box. Interested parties can contact the LASSO PI (william.gustafson@pnnl.gov) if they would like access to the specific code used for this release.

2.2 Large-scale Forcing, Surface Fluxes, and Initial Conditions

Initial profiles and surface forcings for the simulations come from multiple sources. Many simulations in the release use 12 UTC soundings for the initial profiles and the observationally-based surface forcing from the VARANAL product, discussed next. Others use profiles and surface forcing from the same data source as the large-scale forcing.

Three different methodologies have been applied for deriving large-scale forcings to drive the LES models. The goal is to provide a vetted ensemble of LES runs for each case based on multiple forcings since the forcings are arguably one of the largest uncertainties for LES modeling. The three methodologies are also supplemented with different forcing region scales to add additional model spread as the best scale may vary from case to case. This is particularly important for days where large variations occur around SGP that get averaged into the overall forcing, which is represented as a single profile that varies on an hourly basis.

VARANAL

The first forcing method is the ARM constrained variational analysis, VARANAL [Xie et al., 2004], which is based on Zhang and Lin [1997] and Zhang et al. [2001]. VARANAL for this release uses the Rapid Refresh (RAP) analyses as a background gridded field that is then optimally merged with ARM and other observations using a variational approach. The standard VARANAL represents conditions over a 300 km region. Packaged with VARANAL is an estimate of surface sensible and latent heat fluxes over the forcing region.

Two versions of the VARANAL surface fluxes were tested for LASSO, which differently merge surface heat flux observations from the energy balance Bowen ratio method (EBBR) and eddy correlation (ECOR) stations. The first calculates the SGP domain averaged surface flux for ECOR and EBBR separately, then average them with equal weight. The second uses a weighted average based on the land surface type represented by each observation. In most cases the results are very similar, and simulations comparing the two rarely differed for the five days that have been the focus thus far. Most of the released simulations use one of the VARANAL-based flux estimates since these are based directly on observations. A handful of the simulations use fluxes directly from the other forcing datasets to examine the overall sensitivity and model behavior when using a fully consistent set of initial conditions, surface fluxes, and large-scale forcing. Note that fluxes from the the non-VARANAL sources are model derived based on the surface schemes from their corresponding host models.

ECMWF

The second forcing method is a dataset derived from European Centre for Medium-Range Weather Forecasts (ECMWF) forecasts. Two methods were tested. One is based on deriving forcing tendencies from the column nearest to SGP, which is the simplest approach that represents the single column spatial extent of about 16 km. The simulations in this release use the second method where large-scale forcing is based on the Diagnostics in the Horizontal Domains (DDH) system, which uses physical and dynamical tendencies directly from the ECMWF Integrated Forecast System model to calculate closed budget terms. This method can more accurately close the moisture and energy budgets, plus it can be done over multiple spatial extents. The two methods produced similar results for the single column scale. Most of the Alpha 1 simulations use a DDH-based ECMWF forcing scale of 413 km. An additional set of simulations have been done with WRF to test forcing scales of 16

km (single column) and 114 km. Note that the spatial scales listed here are average side dimensions based on the square root of the forcing domain area; the DDH domains are defined with longitude and latitude.

MS-DA

The third forcing method is to derive the large-scale forcing from WRF simulations constrained using the multiscale data assimilation (MS-DA) methodology developed by Zhijin Li [Li et al., 2015a; Li et al., 2015b; Li et al., 2016]. MS-DA is implemented using the community-based Gridpoint Statistical Interpolation (GSI) data assimilation in conjunction with a scale separation algorithm to combine observations representing coarse and fine scales to accurately reflect the atmospheric state. It leverages the large-scale fields from existing reanalysis or forecast produced by operational centers, but constrains small-scale fields by assimilating specialized ARM observations and extracting small-scale information from satellite measurements and observations of other meteorological observing networks.

In the case of LASSO, the MS-DA is carried out on a nested region over the Central United States with the finest grid using 2 km grid spacing for the SGP region. The 2 km grid spacing offers the flexibility of generating large-scale forcing for selected area sizes [Feng et al., 2015]. In the released cases, the areas for 75 km, 150 km and 300 km are used for examining the sensitivity of large-scale forcing to the selected area sizes. Since clouds and precipitation are not directly constrained by data assimilation, the generated large-scale forcing is sensitive to the microphysics used in WRF. The Morrison and Thompson microphysics are used. In the 2015 cases, the assimilated ARM observations include ARM radiosonde soundings and AERIoe profiles of temperature and moisture from the Central Facility, and temperatures and moistures from the MET stations from across the site. Additional measurements included in the assimilation process include NOAA operational observations and satellite radiances.

3 Evaluation Data

Simulations are evaluated using ground-based ARM observations and retrievals of boundary layer cloud and thermodynamic properties. This section describes the observations used thus far, and the next section describes the diagnostics and metrics. As discussed below, a meaningful comparison between observations and model output requires that they be co-registered on the same spatial and temporal grid and processed, as necessary, such that an apples-to-apples comparison may be made between a mode-comparable observational quantity and an observation-comparable model quantity. Some of the methodology is based on Appendix B in Vogelmann et al. [2015]. The Alpha 1 release provides 1 h averages for model-observation comparisons unless otherwise noted. Observations at native resolution are available by request. In future releases, shorter averaging periods will be considered, the variable list will be expanded, and uncertainties included.

In-cloud liquid-water path (LWP)

In-cloud LWP (g m^{-2}) is based on a new product that merges two ground-based LWP retrievals into a single, hybrid LWP dataset that has excellent sensitivity at low LWP (<40 g m^{-2}) and a full dynamic LWP range (up to 1000 g m^{-2}). Clear-sky screening is applied to the observations and simulations in a consistent manner so that only cloud values are used in the averaging (*i.e.*, it is not a domain-averaged, all-sky value). Only retrievals from a single site at the SGP central facility are currently available, which will be expanded in future releases. (See the Appendix for further details.)

1-D Boundary layer cloud fraction (1-D CF)

Two estimates of boundary layer cloud fraction below 5 km are used to approximate the measurement uncertainty of the value experienced at the surface. One is the hemispheric sky cover from the total-sky imager (TSI), and the other is a column measurement of the cloud frequency of occurrence derived from the ARM Active Remote Sensing of Clouds (ARSCL) product [Clothiaux et al., 2000], which uses radar and lidar measurements to generate a vertically resolved cloud mask for the narrow column above the instruments. Cloud fraction is computed from the simulations in a manner that follows from the computation of in-cloud LWP

(described in the Appendix). For the Alpha 1 release, the recommended 1-D CF measurement is from the TSI, as cloud above the boundary layer have negligible impact on CF for the cases provided when boundary layer cloud is present. CF from ARSCL will be improved in a future release by applying an ARSCL simulator to the simulations for a better apples-to-apples comparison. (See the Appendix for further details.)

2-D Cloud mask

2-D cloud masks of the time-height location of cloud are used to assess the simulated cloud-base height, approximate vertical extent, and timing of cloud onset and decay. The observed cloud mask is generated from the ARSCL product, where cloud fractional occurrence is determined for 15 min windows and frequencies greater than zero are masked as being cloud. The current cloud mask for simulations is obtained from grid cells with total hydrometeor mixing ratios greater than 1e–7 kg kg^{-1}. The presence of water cloud is relatively insensitive to this mixing ratio threshold value, but the presence of cirrus clouds is much sensitive to the threshold.

The cloud masks available in the Alpha 1 release are useful for assessing the gross features of the simulated vertical distribution of cloud, but caution should be used to not over interpret the results. This comparison assumes that the frozen turbulence assumption is valid, where the clouds sampled in the narrow column above the instruments is representative of the cloud field, which becomes more problematic for lower values of the 1-D CF. Boundary layer cloud tops may also be difficult to observe adequately due to their low radar reflectivity and possible insect contamination [Lamer and Kollias, 2015]. Future releases will apply an ARSCL-simulator to simulations. Also, use of scanning cloud radar data will be explored to provide improved sampling of the 3-D volume above the SGP.

Lifting condensation level height

The lifting condensation level height (LCL, m) is determined from continuous surface-air observations of relative humidity and temperature as the altitude where the surface-air moisture equals saturation following a dry-adiabatic ascent. A point value is computed from the MET observations at the ARM central facility and the same calculation is applied to the lowest air layer in the simulations, enabling a consistent observation-model comparison. Future LASSO releases will include other surface sites in an areal average.

Surface temperature and moisture

The SGP central facility MET station provides continuous measurements of surface air temperature, $T_{surface}$ (K) and moisture in the forms of mixing ratio, $QV_{surface}$ (g kg^{-1}), and relative humidity, $RH_{surface}$ (%) that are compared to values from the lowest model layer. Future releases will include other surface sites in an areal average.

Mid-Boundary layer moisture and temperature

Raman lidar measurements provide high frequency vertical profiles (~75 m every 10 min) of the boundary layer water vapor mixing ratio, temperature, and relative humidity up to cloud base. Values are used from a height range of 900–1100 m above ground level except for the 29-Aug-2015 case where the range is 600–800 m. The values are averaged using a one-hour moving window to produce mid-boundary-layer-averaged water vapor mixing ratio, $QV_{boundary\_layer}$ (g kg^{-1}), temperature, $T_{boundary\_layer}$ (K), and relative humidity, $RH_{boundary\_layer}$ (%). These values are compared to the simulated values within the same range. (See the Appendix for details.)

Boundary layer thermodynamic profiles

Simulated thermodynamic profiles are compared to the lowest 5 km of the atmosphere observed by soundings at sonde launch times and Raman lidar profiles of temperature and water vapor mixing ratio. Future releases will include a continuous comparison of the boundary layer structure from the Raman lidar.

4 Diagnostics and Skill Scores

The evaluation data are used to assess model behavior using diagnostic plots and quantify model performance using skill scores. Diagnostics plots display comparable observed and simulated values that have been co-registered on the same spatial and temporal grid, and may be accompanied by basic statistical quantities (*e.g.*, mean, root-mean-square (RMS), etc.). Skill scores are metrics that quantify the model performance seen in the diagnostic plots such that simulation quality can be numerically compared to one another for different variables. Data files and quicklook plots of the diagnostics and skill scores are available within the data bundles, and a set of key skill scores are used in the LASSO Bundle Browser for users to find and select simulations based on their performance (see LASSO Data Bundles and Tools).

4.1 Diagnostic Plots

Heat maps provide in a single plot an overview of model performance of a variable for all simulations within a case day. An example is given in Figure 1 where the magnitude of the model-observation differences are provided for each grid and color coded. Heat map quicklooks (.png) are generated for: LCL; CF(ARSCL); CF(TSI); LWP; boundary layer Qv, RH, T; and surface Qv, RH, T. They are available for display within the data bundles using "heat_maps.html" located one level below the date directory:

http://iop.archive.arm.gov/arm-iop-file/0eval-data/gustafson/lasso-alpha1/YYYYMMDD/metrics/heat_maps.html

where YYYYMMDD is the case date.

A series of other quicklook diagnostics plots are used to compare specific simulations to observations. Examples are given in Figure 2. They are available for display within the data bundles using "plots.html" located one level below each simulation directory:

http://iop.archive.arm.gov/arm-iop-file/0eval-data/gustafson/lasso-alpha1/YYYYMMDD/sim####/obs_model/plots.html

where YYYYMMDD is the case date and #### is the four digit number of the simulation.

Top panel

Contains plots of time series, Taylor diagrams, and regressions. Diagnostics plots are available for: LCL; CF(ARSCL); CF(TSI); LWP (linear y-axis); LWP (log y-axis); boundary layer Qv, RH, T; and surface Qv, RH, T. The time series are accompanied by simple statistics: means of the observations and simulation, ratio of the means (Sim/Obs), mean difference (Sim-Obs), RMS difference, and correlation coefficient. Taylor diagrams graphically summarize how closely a pattern matches observations in terms of their correlation and normalized standard deviation [Taylor, 2001]. A perfect match of these terms in polar coordinates is at (1,1) (although, as discussed in the next section, one must also consider the mean bias). The regression plots provide the slope (m) and intercept (b).

Lower-left panel

Contains the 2-D time-height cloud frequency of occurrence derived from ARSCL observations, the LES simulation, and 2-D cloud masks from the ARSCL observations the simulation. In the latter, green indicates where the simulation and observations both have cloud (model hit), red is where cloud is present only in the observations (model miss), and blue is where cloud is present only in the simulation (model false positive). Local solar time is indicated at the top and UTC at the bottom. A two-toned vertical scale is used where the vertical region below 5 km is expanded and above 5 km is reduced to show the full tropospheric cloud profiles without sacrificing details of the boundary layer clouds; the partition between the regions is indicated by a dashed line. Note that at this time the simulations have not been processed by an ARSCL simulator, which will be done in a future release. Also included is the observed LCL (blue line), and computations from the sonde profiles of the level of free convection (LFC, red +) and boundary layer height from the Heffter [1980] method (green *).

Lower right panel

Contains comparisons of the simulations to available sonde profiles at ~11:30 solar time, ~14:30, and ~17:30. The quantities compared are temperature, T (K), water vapor mixing ratio, qv (g kg^{-1}), potential temperature, θ (K), and equivalent potential temperature, θ_e (K). Also included are the Raman lidar profiles of temperature and water vapor mixing ratio above 300 m.

4.2 Skill Scores

Skill scores quantify model performance compared to observations. They monotonically increase with improved skill from 0 to 1, where 0 indicates no skill and 1 indicates perfect agreement in terms of the metric. LASSO draws as much as possible on skill scores commonly used within the community. The purpose for providing the skill scores is to help users find cases of suitable quality for their applications. As there may be a cluster of simulations with high skill scores for a given variable, there may be several suitable simulations that exceed a desired threshold. However, that number may dwindle as skill scores are considered for other variables important for the application of interest. Thus, the purpose of the skill scores is not to identify a "best" simulation, as what is best may depend on the application; rather, the purpose is to identify the "better" cases for consideration.

Time Series Skill Score

Model performance in terms of its time series is quantified using two skill scores, where one characterizes the agreement of the variation/shape of the time series and the other characterizes its mean. The Taylor skill score (equation 4 in Taylor [2001]), S_T, is used for the variation/shape of the distribution for a given variable, var (*e.g.*, LWP), as

$$S_T(var) = \frac{4(1+R)}{\left[\left(\sigma_r + \frac{1}{\sigma_r}\right)^2 (1+R_0)\right]} \tag{1}$$

where σ_r is the normalized standard deviation given by model RMS divided by the observed RMS, R is the correlation coefficient, and R_0 is the maximum correlation attainable which is set to 1. Thus, if the correlation coefficient and normalized standard deviation are 1 the Taylor skill is 1. However, the Taylor skill alone cannot characterize the time series performance because it does not include information regarding the mean. To include this information, a skill score for the relative mean, S_{RM}, was developed as

$$S_{RM}(var) = \begin{cases} x \text{ for } x \leq 1 \\ 1/x \text{ for } x > 1 \end{cases} \tag{2}$$

where x is the model mean divided by the observed mean. Through this formulation, the skill score has the range [0,1] and is symmetric around one. It is designed to quantify the relative difference from 1 and will yield the same value if the model underestimates or overestimates by the same factor. For example, two relative means that are different from observations by a factor of 2 on the low and high side, *i.e.*, relative means of 0.5 and 2.0, would have the same skill score of 0.5 implying comparable performance relative to 1. Should a user want examine the relative means themselves, they are also included in the data bundles.

The Taylor and relative mean skill scores may be used in scatter plots to show how different simulations behave. See Figure 3 for an example. The closer the values are to the upper right-hand corner (1,1) the better the model performance in terms of the time series variable.

Finally, we found it useful to combine the Taylor and the relative mean skill scores into a single-variable net-skill score, S, that quantifies how close a simulation is to (1,1) in Figure 3. To do so, we use

$$S(var) = \left(S_T(var) * S_{RM}(var)\right)^{\frac{1}{2}} \tag{3}$$

In this way, should the Taylor skill and relative mean skill both be 0.8, the combined single-variable net-skill score would be returned as 0.8. This multiplication is preferable to, say the square root of the sum of the squares,

because it requires that both skill scores perform well for S to rank well; it does not allow a high score in one term to compensate for a much lower score in the other term. For example, if there were two sets of skill scores (0.5, 0.5) and (1, 0.1) the former would score better using equation 3 while the latter would score better with the square root of the sum of the squares. Note that while high net-skill scores can only be achieved by having both high Taylor and relative mean skills, medium-to-low values need not have the same level of consistency in their component skill scores since multiple combinations of high and low scores can yield the same net score.

2-D Cloud Mask Skill Score

The 2-D cloud mask in Figure 4 shows the ability of the model to simulate cloud-base height, vertical cloud extent, and the timing of cloud onset and decay. (As previously mentioned, application of an ARSCL simulator is in progress that will enable a closer comparison of the simulated cloud fields to ARSCL observations.) The skill for the simulated 2-D mask is quantified using the frequency bias and the Equitable Threat Score (ETS), also called the Gilbert skill score [Mesinger and Black, 1992; see "Forecast Verification Metrics" at https://hwt.nssl.noaa.gov/Spring_2012/],

$$ETS = \frac{(Hits - Hits_{random})}{(Hits + Misses + False\ alarms - Hits_{random})} \tag{4}$$

The ETS skill score is only applied to cloud below 5 km as boundary layer clouds are the focus of this release. In this equation, *Hits* is the number of cloud pixels both correctly simulated and observed (green in bottom-left panel in Figure 2), *Misses* is the number of cloud pixels not simulated but observed (red), and *False alarms* is the number of cloud pixels simulated but not observed (blue). $Hits_{random}$ is the number of hits that might happen at random, given by,

$$Hits_{random} = \frac{(Hits + False\ alarms)(Hits + Misses)}{Total} \tag{5}$$

where *Total* is the total number of pixels below 5 km. ETS has the range of –1/3 to 1, where 0 indicates no skill. To have ETS conform to our other skills scores that are within the range [0,1], we truncate the low end of ETS at 0 and refer to it as the truncated ETS skill score, S_{ETS}.

The ETS-related frequency bias is the ratio of the frequency of simulated cloud pixels to the frequency of observed cloud pixels,

$$Bias = \frac{(Hits + False\ alarms)}{(Hits + Misses)} \tag{6}$$

The frequency bias is in terms of a ratio where a perfect score is 1; so, following the approach used to compute the skill for the relative mean, the skill score for the frequency bias, S_{Bias}, may be computed by replacing x in Eq 2 with with Bias from Eq 6. The skill score is referred to as the frequency bias skill.

These two skill scores may be used in scatter plots to show how different simulations behave in terms of 2-D cloud mask. See Figure 4 for an example. Generally speaking, simulations usually score better in terms of frequency bias skill than in ETS skill. While ETS skill can be a rather exacting skill score compared to its peers, it has the virtue of not giving errantly high values (*i.e.*, a high value can be believed) and awarding values more consistent with visual inspections of plots.

Similar to the time series metrics, we find it useful to combine the ETS skill score with the frequency bias into a single-variable net-skill score, S(2D), that quantifies how close a simulation is to (1,1) in Figure 4,

$$S(2D) = (S_{ETS} * S_{Bias})^{\frac{1}{2}} \tag{7}$$

Multivariable Net-Skill Score

The advantage of having a net-skill score for a variable (equations 3 and 7) is that it allows comparison of the net-skill scores for two variables in scatter plots. An example is in Figure 5 for a comparison of the net time-series skill scores for LWP and CF(TSI). As for Figure 3, the closer the values are to the upper right-hand corner the

better the model performance. The values for two net-skill scores may be combined into a single multivariable net-skill score similar to equation 3,

$$S(x,y) = \left(S(x) * S(y)\right)^{\frac{1}{2}} \tag{8}$$

where S(X) and S(Y) are the net-skill scores for two variables. The multivariable net-skill score for LWP and CF(TSI), S(LWP,CF(TSI)), is considered to be a special case that is referred to as the *1-D cloud skill score*.

Following equation 8, it is also possible to combine a single variable net-skill score with a multivariable net-skill score. For example, we combine the 1-D cloud skill, S(LWP,CF(TSI)), with the 2-D mask net skill, S(2D), to produce one skill score that characterizes model performance of the LWP and CF(TSI) time series *and* the 2-D cloud mask,

$$S(S(2D), S(LWP, CF(TSI))) = (S(2D) * S(LWP, CF(TSI)))^{\frac{1}{2}} \tag{9}$$

This is a special case that is referred to as the *total cloud skill score*.

We note that while one could continue to combine more multivariable skill scores using equation 8 in series, one should be cautioned about diminishing returns. As noted earlier, a high net-skill score can only be obtained by having two high input values, but the reason for a low skill score becomes more ambiguous since there are nonunique paths to the same low value. As more variables are added, the likelihood of a low score increases and, along with it, the ambiguity of comparing two low scores.

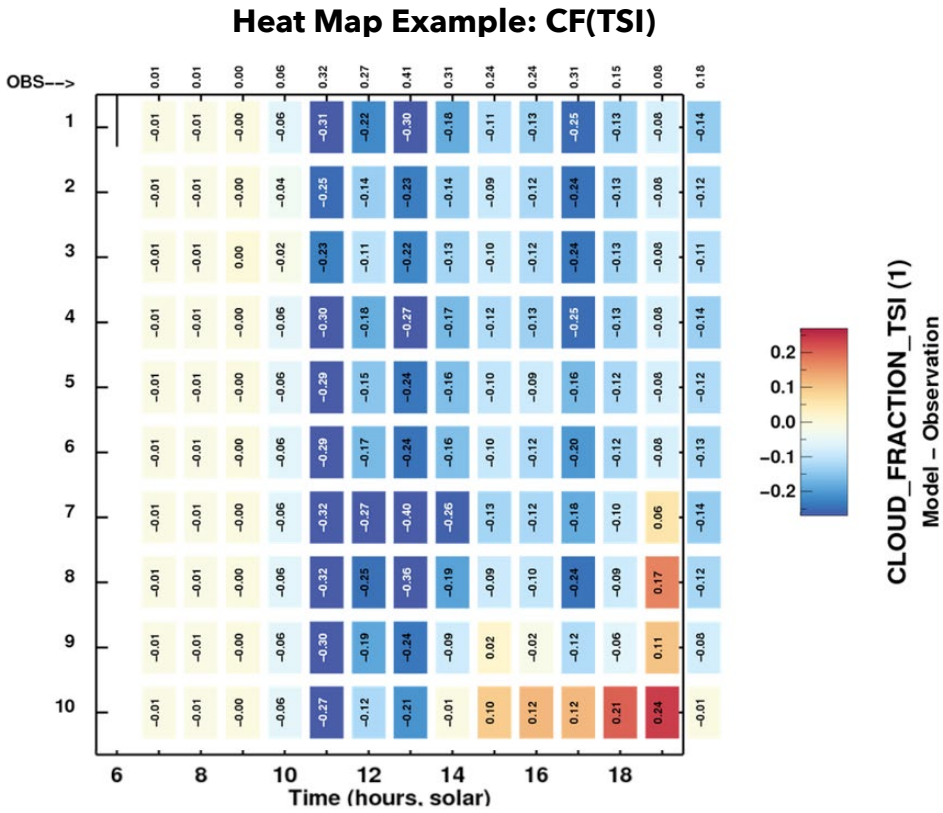

Figure 1. Heat map example of simulated cloud fraction compared to the TSI for the 27-Jun-2015 case. Simulation number is given by the left column and the local, solar time is given at the bottom. The top row gives the observational mean for each hour and the last value outside the box is the daily mean. The grid provides the corresponding differences of the simulated values (model-observation) that are color coded by the key given at the right.

Diagnostic Plot Examples

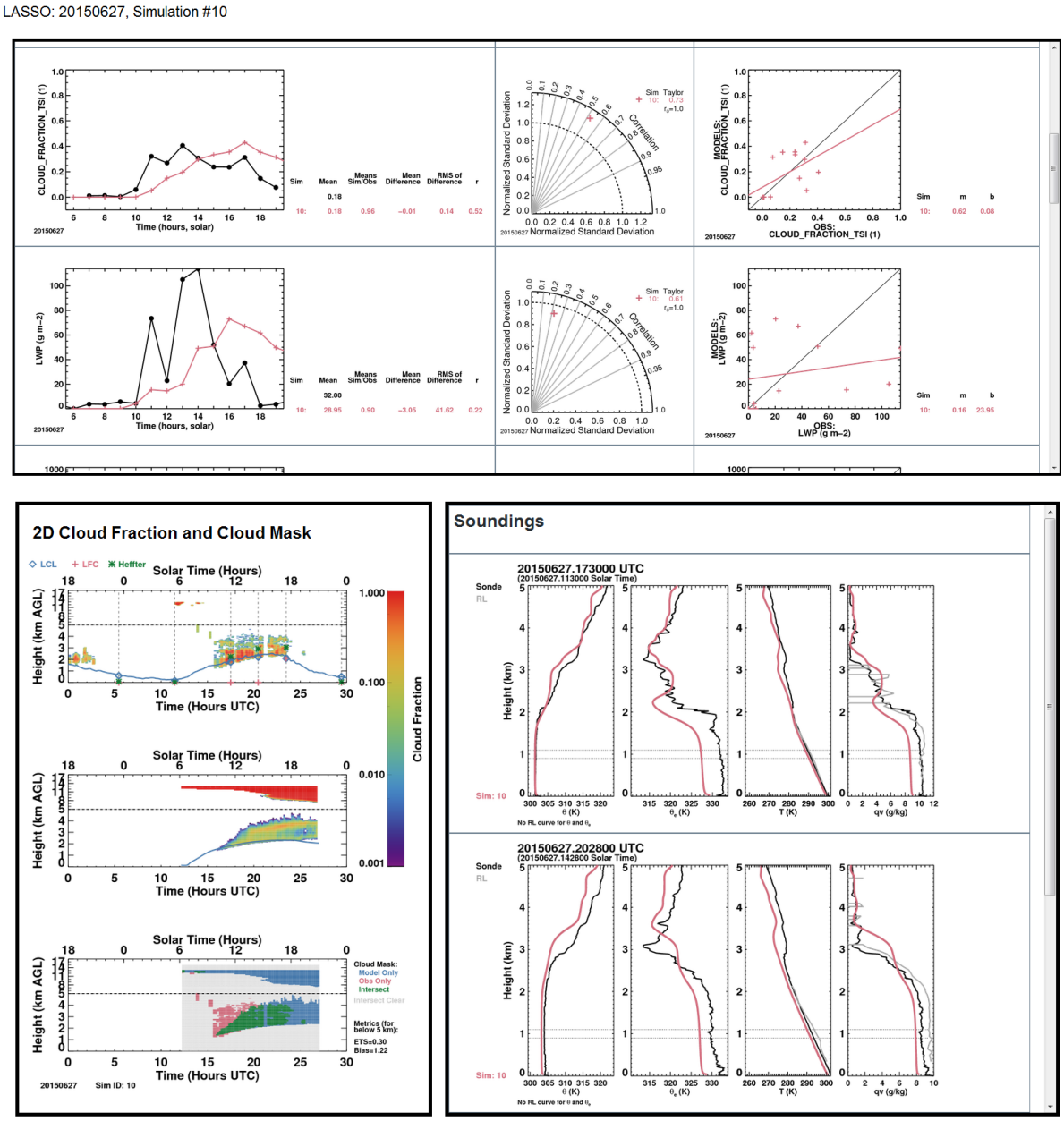

Figure 2. Example of diagnostic plots available for each simulation within the data bundles (see text for details). (Top panel) Quicklooks are available for various time series, Taylor diagram, and regression plots. (Bottom-left panel) Top plot is the 2-D time-height cloud frequency from ARSCL, middle is from the simulation, and the bottom is the 2-D cloud masks from ARSCL and the simulation. (Bottom-right panel) Comparison of simulated profiles with those from sondes and the Raman lidar.

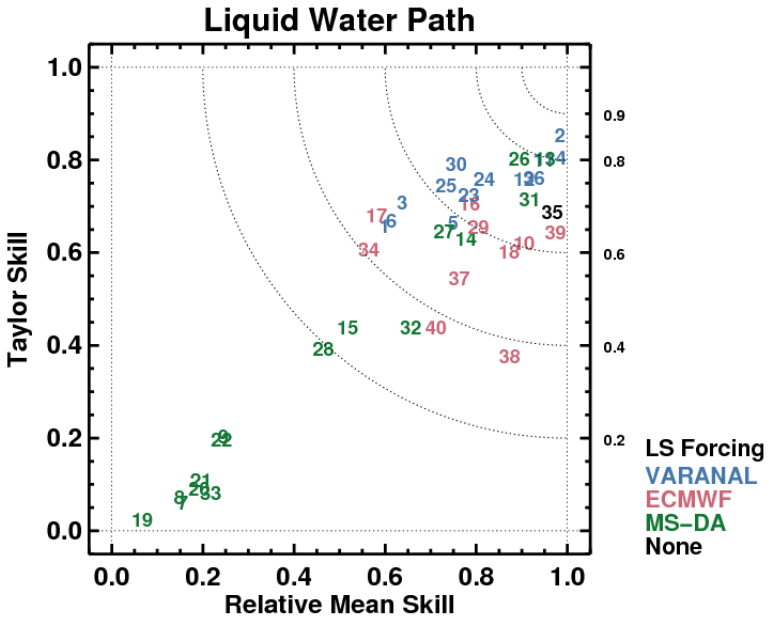

Figure 3. Scatter plot of LWP Taylor skill score, S_T(LWP), and relative mean skill score, S_{RM}(LWP), obtained from their time series comparison to observations. Each point represents a simulated day and the numbers indicate the simulation ID. Colors indicate the large-scale forcing used as indicated in the legend, where "none" is a simulation without large-scale forcing. The 40 simulations shown are from the 27-Jun-2015 case. Dashed curves are for constant values of net-skill scores, *S*(LWP), notated at the right axis. The closer a point is to the upper right-hand corner (1,1), the better the simulation performance for this metric.

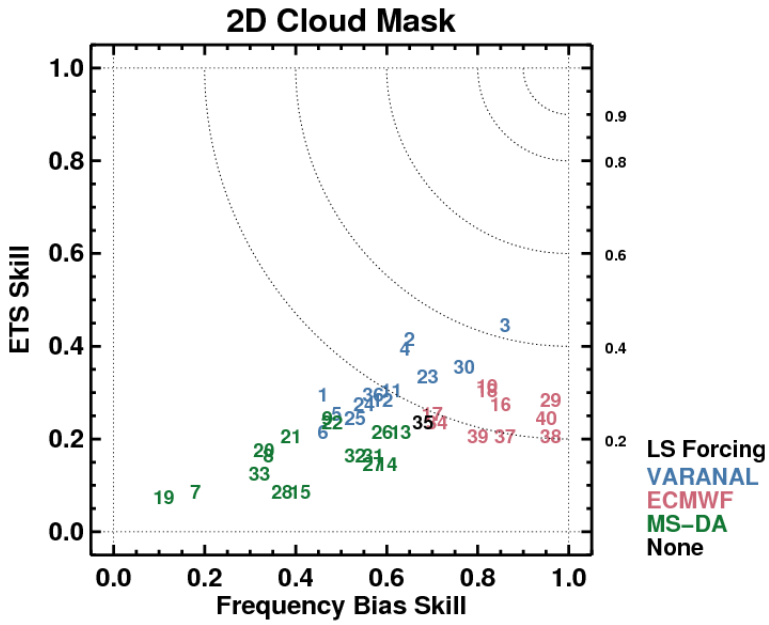

Figure 4. As for Figure 3 but for 2-D cloud mask skill scores of ETS skill, S_{ETS}, and frequency bias skill, S_{Bias}. S_{ETS} is often lower than other skill scores, but this happens uniformly such that a low S_{ETS} could have comparable visual agreement with a higher time series skill score, *e.g.*, *S*(LWP).

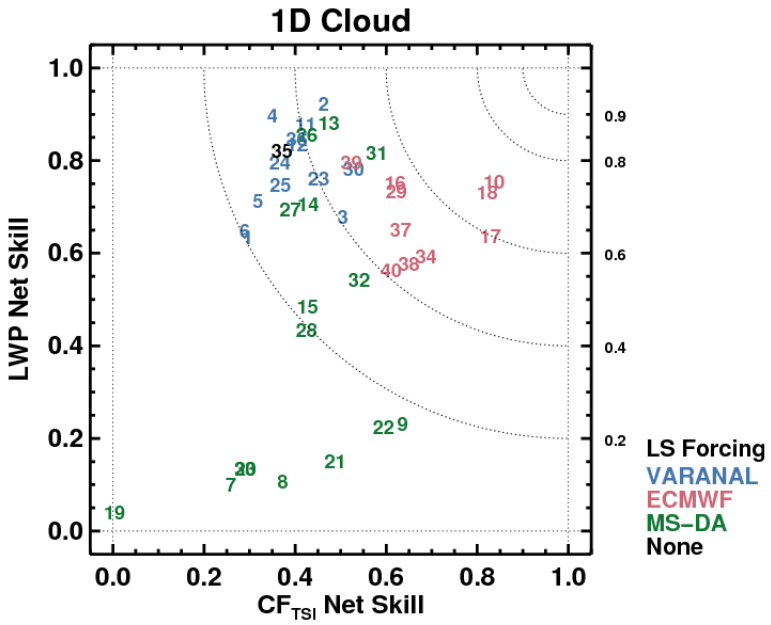

Figure 5. As for Figure 3 but for two single variable net-skill scores, *S*(LWP) and *S*(CF(TSI)). In this way simulation performance for two separate skill scores can be visualized. Should equation 8 use these two skill scores as input, it would result in a single multivariable-net-skill score for each pairing, *S*(LWP,CF(T-SI)), that is referred to as the *1-D cloud skill score*.

5 LASSO Data Bundles and Tools

The overall concept for data organization within LASSO is the use of "data bundles." Each bundle is associated with a single simulation and contains the information necessary to repeat the simulation, the output from the simulation, subsetted output co-registered with observations, and the metrics and diagnostics for evaluating the simulation. The Alpha 1 release also contains an initial version of a web tool for quickly searching through simulations by querying metric values and configuration details.

5.1 Organization of the File Structure

The file structure for the Alpha 1 release is shown schematically in Figure 6 and Figure 7. The highest level directory *lasso-alpha1* contains a *docs* directory and a directory for each of the five case dates. The *docs* directory contains this documentation file, a spreadsheet listing all the Alpha 1 simulations, and other pertinent descriptive information. The *lasso-alpha1* directory also contains directories for each case date, which are named using the format *YYYYMMDD*. These case date directories contain a *metrics* directory with overview metrics that cross all simulations within the case, and separate directories for each simulation's "data bundle." These simulation directories, *sim####*, contain a *config* directory that holds model inputs and configuration files, an *obs_model* directory that contains subsetted model output and observations that are coregistered in space and time, and a *raw_model* directory that contains the basic model output. Model output is segregated into instantaneous fields of typical model output, such as the state variables, and diagnostic domain statistics, which mostly entail time series of domain-averaged profiles. The file naming conventions are consistent for most of the directories except for the configuration files and raw model output, which vary based on whether they derive from the WRF and SAM models.

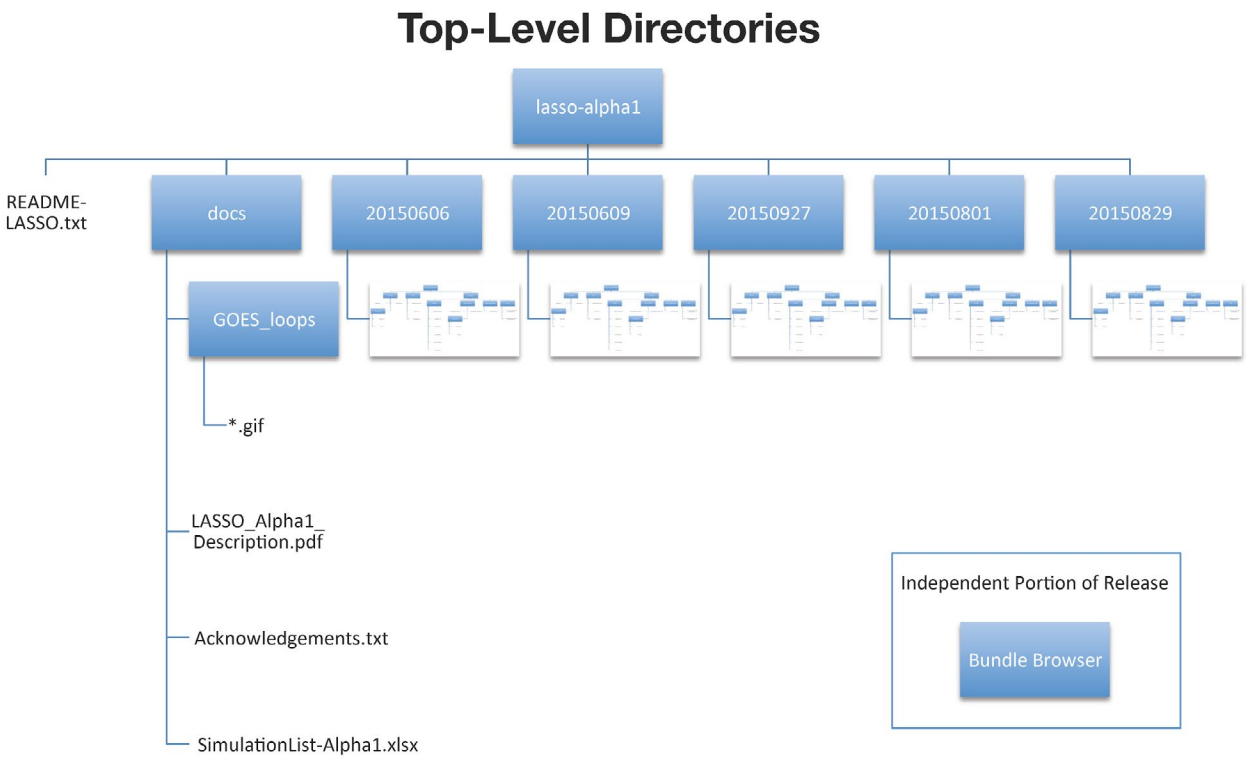

Figure 6. Schematic of top-level directory structure.

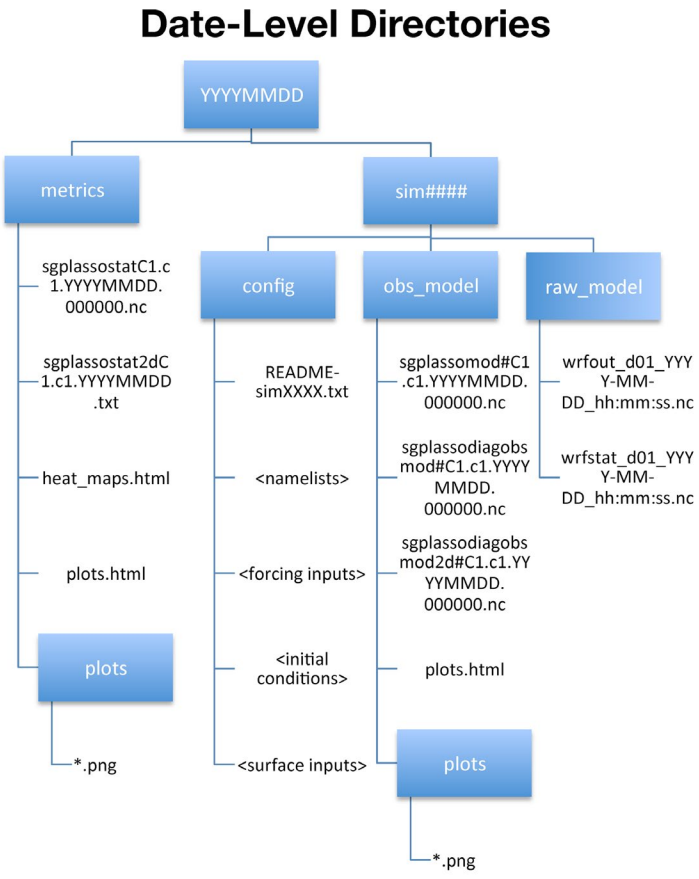

Figure 7. Schematic of the directory structure for each case date.

The SAM and WRF models output in different formats with different variable names. We have chosen to output the statistics variables for the models as separate files since these are time-averaged instead of instantaneous outputs.

The SAM model initially outputs in binary, which is then converted to netCDF, and the variables are split between a 3-D file with instantaneous fields, a 2-D file with instantaneous output, and a statistics file that contains domain-wide statistics that render as profiles at each output time. Note that most of the statistics files are time averaged over a 10-min period, with sampling every minute. Some of the older simulations use a different averaging period as indicated in the files. *Note that the time label for these SAM statistics files represents the middle of the averaging period*. The instantaneous output has time labels corresponding with the timestep when the output occurs.

In our current configuration, the WRF model outputs all variables into a single file. We then use the NCO ncks utility to split the original output into a wrfout_d01_<timestamp> file that contains the instantaneous output and a wrfstat_d01_<timestamp> file that contains the time averaged output. Similar to SAM, the WRF statistics are time averaged over a 10-min period with sampling done every minute for most simulations. Some older simulations use a 15-min averaging period. Note that the time label for the time-averaged WRF output differs from SAM. *For WRF, the time stamp label for time-averaged variables is at the end of the averaging period.*

Details regarding the contents of the files are provided in the accomapnying file, "File Contents for the LASSO Alpha 1 Release," that contains header dumps of the netCDF files.

5.2 The LASSO Bundle Browser

The LASSO Bundle Browser provides an interactive web interface for users to find simulations of interest through examination of the LES performance relative to select ARM observations. It allows users to visualize the LASSO data bundle diagnostics and skill scores on the fly using plots and tables while also providing links to data. Values for plots and the data table are fetched dynamically from a Cassandra NoSQL database. The conditional query to retrieve data is formed based on the user selected traits in the browser.

The LASSO Bundle Browser is available for use at http://archive.arm.gov/lassobrowser. Figure 8 shows an example of the display. The left-hand side is occupied by selection options within (A), (B), and (C) whose results are displayed to the right. The selection options and display features are described below referencing the labeling in Figure 8.

A. Expandable menus allow the user to select a single date and measurement type for any combination of traits that characterize the forcing and model configurations. "Select all" is an option within each category and the "Select All" button at the top of (A) selects all forcing and model configuration options. Clicking the "Submit" button at the bottom of (A) displays the results in (D) in the forms of Taylor diagrams, skill score plots, scatter plots, and time series plots that are created using the D3.js and highcharts software libraries. A data table (E) also displays the skill scores for the selected measurement and date.

B. Precomputed overview plots for all simulations and variables for a selected day are available for display for heat maps (Figure 1) and skill score metrics (*e.g.*, Figure 3–5). These overview plots can assist users to locate the variables of interest for use in (A).

C. Slide rulers allow choosing the range of net skill scores that are displayed in (D) and (E). Place the mouse over the label for a brief description of the variable.

D. The date and measurement selected are given at the top of (D) for the displayed plots, which are Taylor diagrams, skill score plots, scatter plots, and time series plots. The black line in the time series plot is the observations. The plots are interactive; mouse over the points to see the simulation ID and coordinate values. Click on a given plot to enlarge and print.

E. The tabulated results are given for the net skill scores in (C) for the selected forcing and model configuration and slide-rule ranges. The "i" to the left of the simulation ID provides a short readme file containing a detailed summary of the simulation run configuration that includes information not available in (A). "Diagnostics" and "Data" hyperlinks are provided at the right of the simulation

ID. “Diagnostics” links to the precomputed diagnostics are given in Figure 2 for that simulation (*e.g.*, 2D cloud mask time series plots, etc.). The “Data” link takes the user to the data download page for that simulation. Arrows at the top of each column order the table entries according to the column variable and the order may be reversed by a subsequent click. The “Search” box finds a given value within the table. Above the simulation ID are options to “print” or “copy” the results or download as “CVS” or “PDF”.

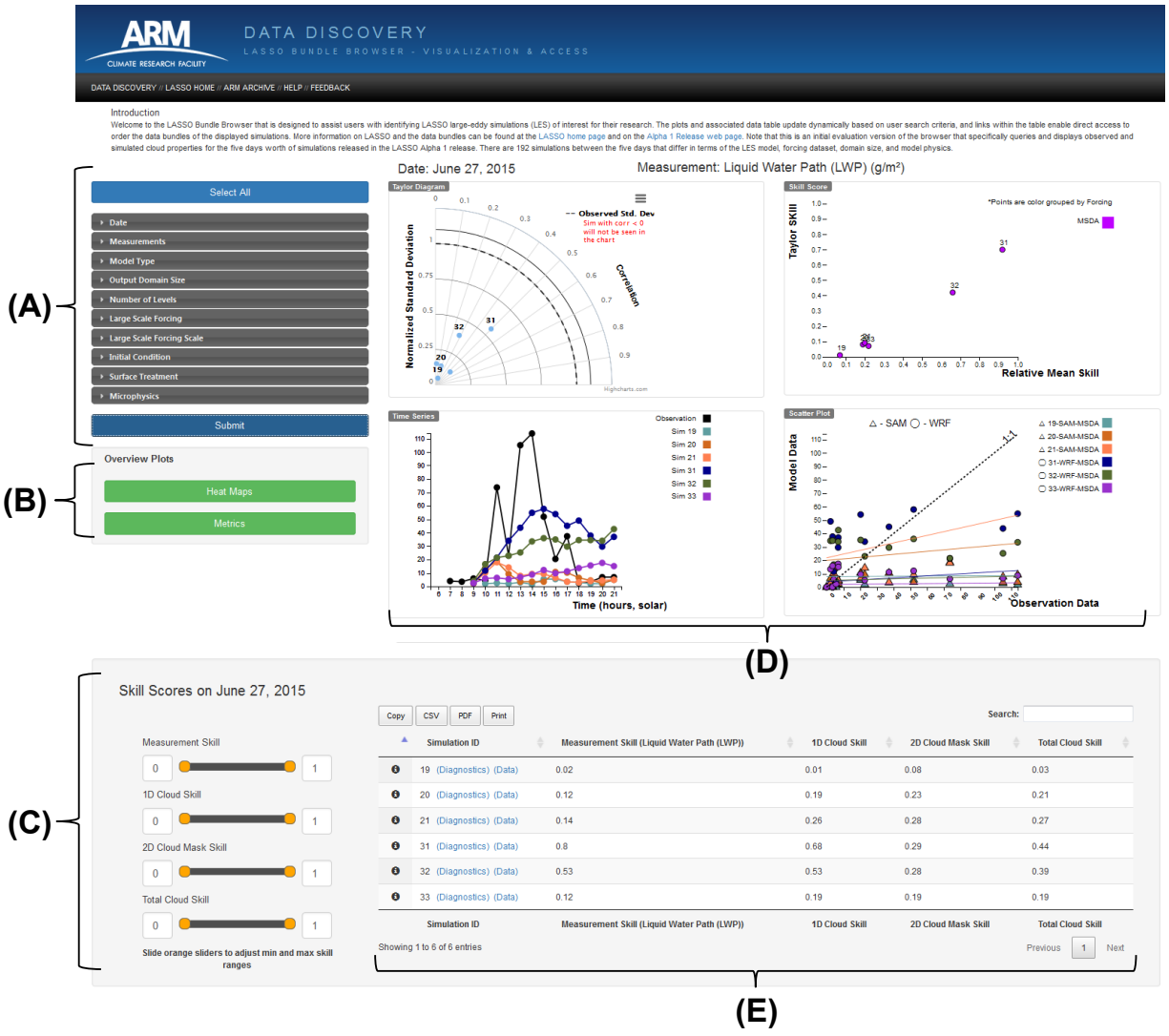

Figure 8. LASSO Bundle Browser interface at http://archive.arm.gov/lassobrowser. See text for descriptions.

6 Alpha 1 Case Descriptions

Five days were chosen during the period June–August 2015 for initial testing of model configurations and forcing calculation methodologies. The primary criteria used to select the cases were that they be classic shallow convective days and that sufficient ARM data be available for each case for forcing and evaluation purposes. The primary measurement products of interest were KAZR-ARSCL, TSI, AERIoe, SONDE, and the Raman lidar. An initial scan of TSI movies revealed days with relevant cloud fractions, which were then verified as shallow convection with KAZR-ARSCL. Days with too much missing data from primary measurements were excluded. The definition of shallow convection was intentionally left somewhat vague to garner a sufficient sample. The resulting search revealed three cases during June, none during July, and two during August. The August days were not strictly classic shallow convection, as they have somewhat complicated, layered cloud conditions with strong synoptic influence. However, it was felt that three days was insufficient to start evaluating initial model configuration and forcing options, so the additional cases were included. Cases during earlier years were not pursued to supplement the 2015 days because of changes to weather forecast models used to generate the forcings and because of changes in available ARM observations. Cases were needed that would be most representative of modeling conditions going forward in time.

The following describes the overall meteorological conditions for each simulated day. The intent is to provide a general context for understanding the overall model behavior. Each case is accompanied by a series of figures illustrating the synoptic conditions and type of clouds present around SGP. Animations of the GOES visible channel for each date are also available within the Alpha 1 evaluation product at http://iop.archive.arm.gov/arm-iop/0eval-data/gustafson/lasso-alpha1/docs/GOES_loops/.

6.1 6-Jun-2015 Case

The synoptic situation on 6-Jun-2015 is dominated by a surface low centered over the Dakotas that propagates from the west side to the east side of the Dakotas during the day. The resulting trough stays to the west of Oklahoma throughout the day and associated cold and warm fronts do not directly impact Oklahoma. The SGP site resides in a ridge to the east of the trough. The flow is southerly at surface and veers to westerly aloft.

The morning sounding at 12 UTC reveals a shallow inversion with an overlying residual layer from the preceding day. By noon, a well-mixed PBL has deepened to entrain the residual layer. The TSI-based cloud fraction shows roughly 20% cloud fraction for most of the day, but this consists of a mix of cirrus in the morning that changes to shallow convection around 16 UTC with a cloud base around 1500 m, that rises to around 2000 m during the day. The GOES animation at http://iop.archive.arm.gov/arm-iop-file/0eval-data/gustafson/lasso-alpha1/docs/GOES_loops/GOES_vis_ict_20150606.gif shows that the cirrus is part of a band that extends to the north and advects east past SGP. The hourly mean in-cloud LWP measured at the Central Facility is <10 g m^{-2} most of the time.

The shallow clouds observed at the Central Facility are only partially representative of the entire region used to generate the model forcings based on the GOES animation and the Aqua and Terra corrected reflectance. SGP lies on the north to northwestern edge of an extensive ShCu region that extends southward into Texas, with clear skies to the west of SGP. Deep convection occurs in the states to the west, north, and east of Oklahoma. Thus, the forcings represent a mix of meteorological conditions that combine clear and shallow cloud environments plus possible influences of deep convective outflows.

Synoptic Conditions for 6-Jun-2015

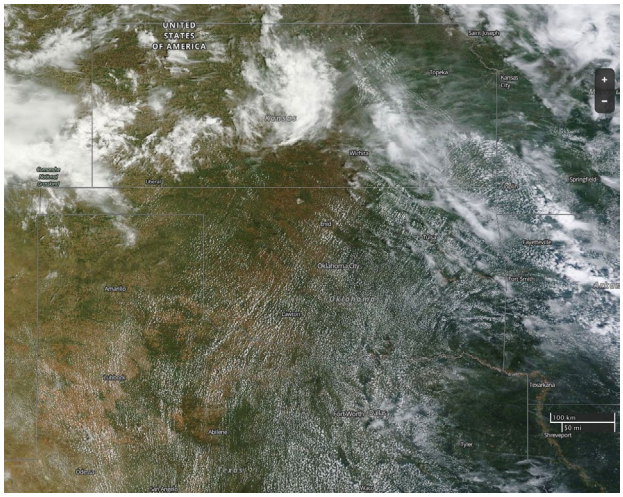

Figure 9. MODIS Terra corrected reflectance for 6-Jun-2015. Acquired from NASA EOSDIS Worldview, http://go.nasa.gov/1OmbCKp.

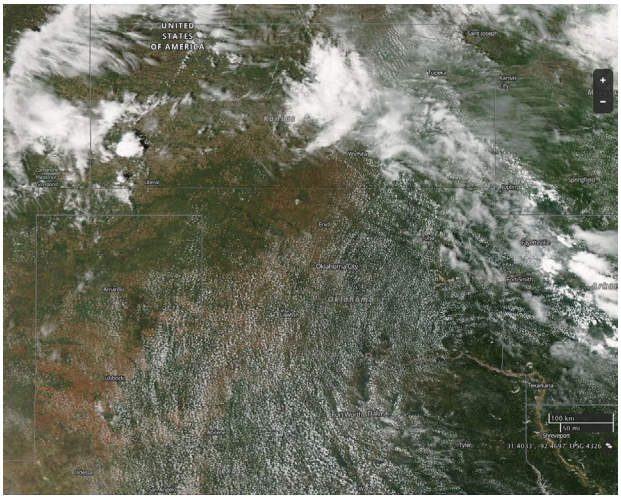

Figure 10. MODIS Aqua corrected reflectance for 6-Jun-2015. Acquired from NASA EOSDIS Worldview, http://go.nasa.gov/1PpDate.

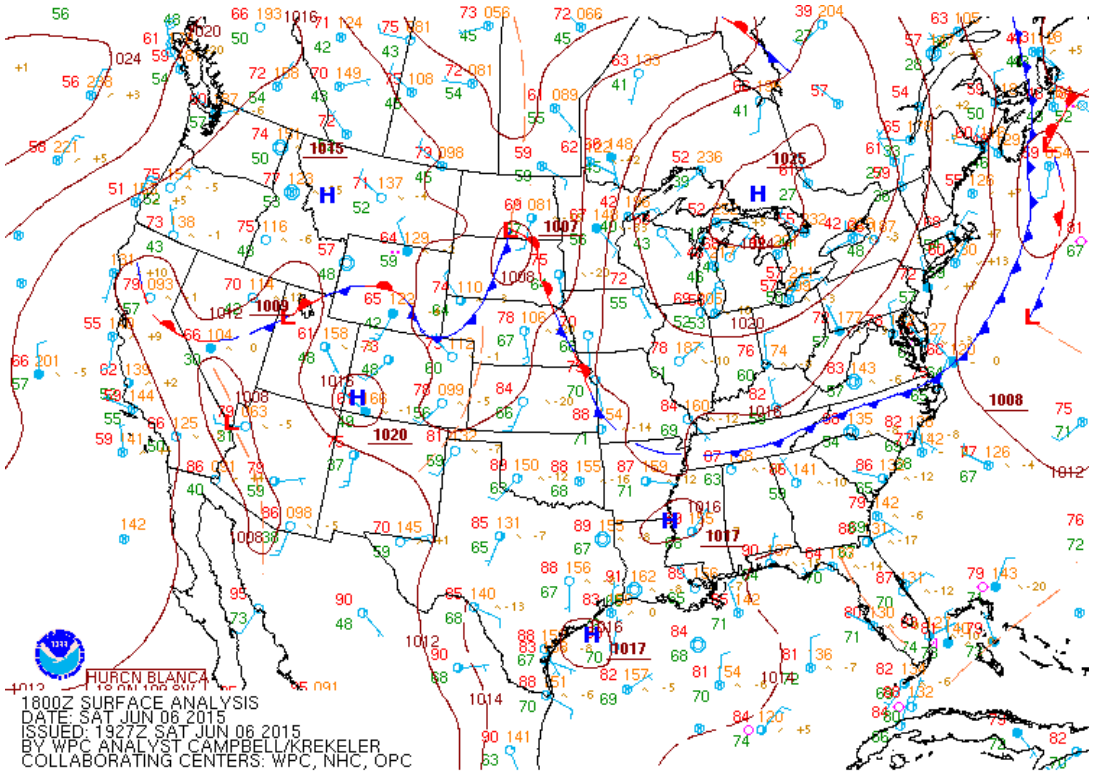

Figure 11. Surface analysis for 6-Jun-2015 18 UTC. Acquired from NWS Weather Prediction Center, http://www.wpc.ncep.noaa.gov/archives/web_pages/sfc/sfc_archive_maps.php?arcdate=06/06/2015&selmap=2015060618&maptype=namussfc.

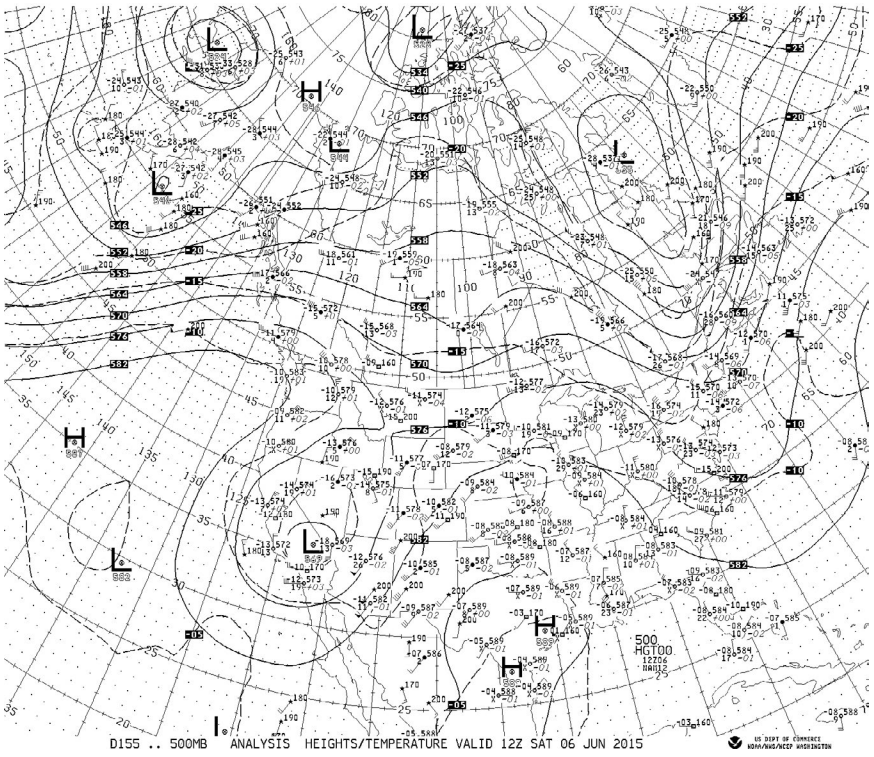

Figure 12. 500 hPa synoptic map for 6-Jun-2015 12 UTC. Acquired from Storm Research and Consulting, http://www.stormresearch.com/ncep/2015/2015_06/20150606122_500.tif.

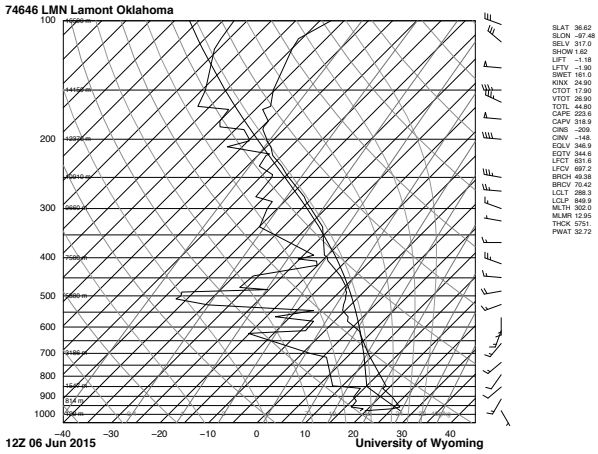

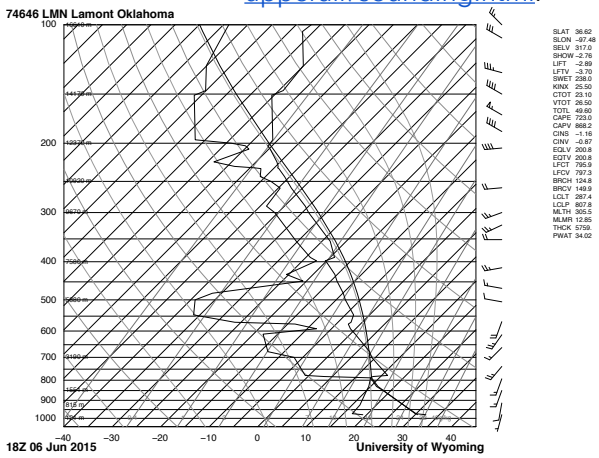

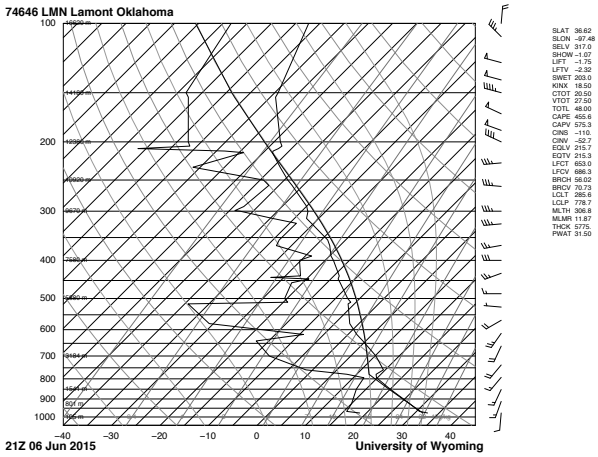

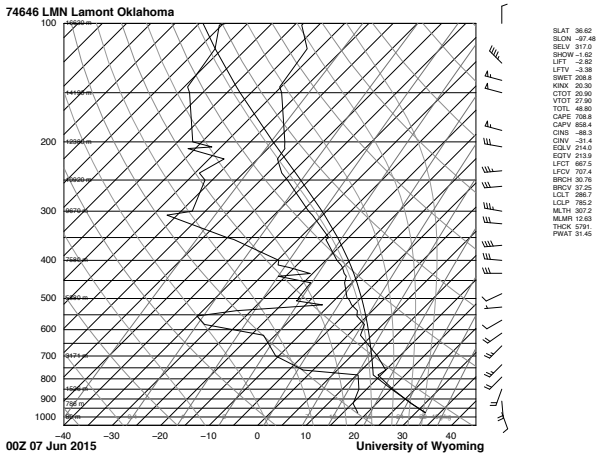

Figure 13. Skew-T log-P diagrams from Lamont, OK for 6-Jun-2015 at 12, 18, and 21 UTC and 7-Jun-2015 0 UTC. Acquired from U. Wyoming, http://weather.uwyo.edu/upperair/sounding.html.

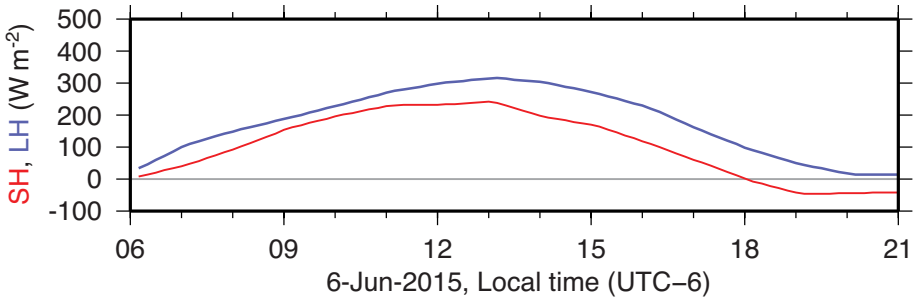

Figure 14. Surface sensible (red) and latent (blue) heat fluxes averaged for the SGP region by weighting fluxes based on percentage of land use type.

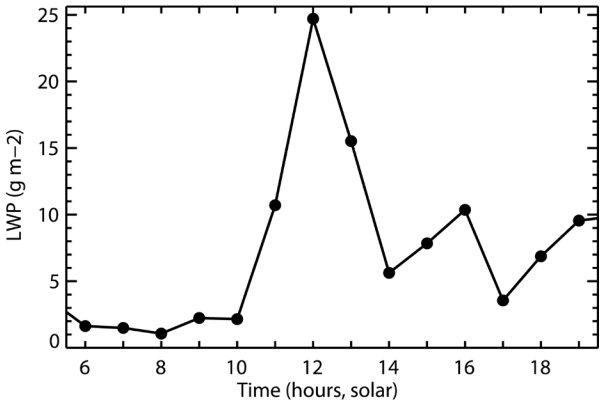

Figure 15. Cloud liquid water path for 6-Jun-2015 at the Central Facility based on MWRRet and AERIoe.

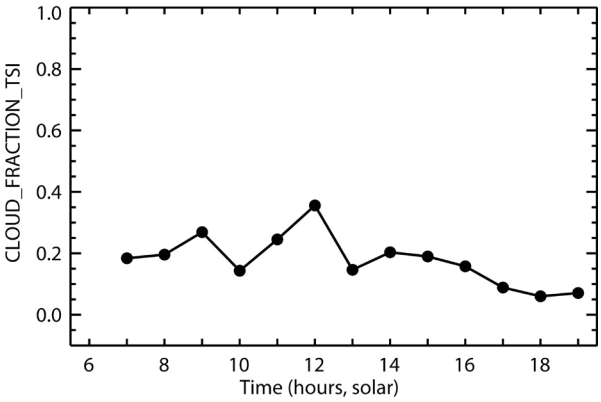

Figure 16. Cloud fraction derived from the TSI for 6-Jun-2015 at the Central Facility.

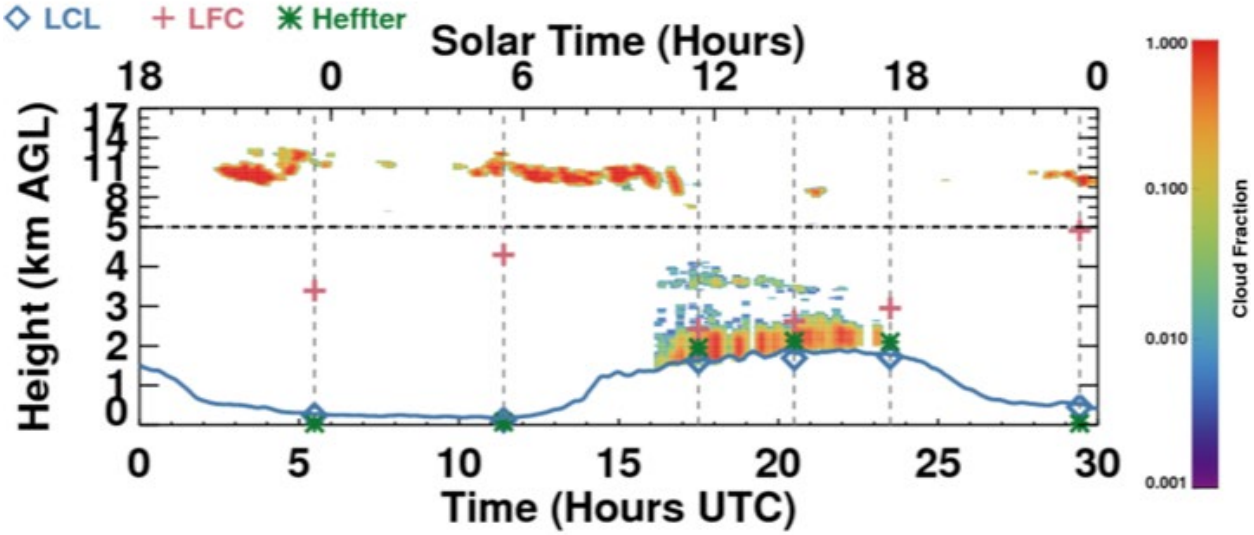

Figure 17. Cloud fraction profiles derived from the KAZR-ARSCL for 6-Jun-2015 at the Central Facility. Note the non-linear vertical axis that emphasizes the lower troposphere. Also indicated are the LCL, LFC, and PBL height based on the Heffter methodology, each of which are calculated from the SONDE product.

6.2 9-Jun-2015 Case

The synoptic conditions at SGP on 9-Jun-2015 are fairly benign and lead to widespread shallow convection throughout much of Oklahoma and Kansas during the day with clearer skies in the eastern portions of these states. A large band of cirrus lies to the south, but is generally far enough away as to not influence the SGP region. The day begins with a stationary front located in southern Oklahoma that dissipates by 18 UTC. The SGP is located near the southern side of a trough that has several shortwaves located throughout the Midwest that propagate eastward. The morning residual layer is at about 700 hPa, which is somewhat higher than on 6-Jun-2015. The temperature within the PBL becomes well mixed by 18 UTC but the moisture profile within the PBL retains vertical structure throughout much of the day. The overall flow is southerly at the surface, veering to northwesterly aloft.

Shallow clouds form around 1730 UTC with cloud fractions around 35% for much of the afternoon. Clouds observed at the Central Facility have a small LWP most of that time, but do exhibit a couple hours ≥50 g m^{-2}. The cloud field is relatively uniform throughout the area used to generate forcings for the LES and clearly impacts the sensible heat flux, which has a flattened time series during midday.

Synoptic Conditions for 9-Jun-2015

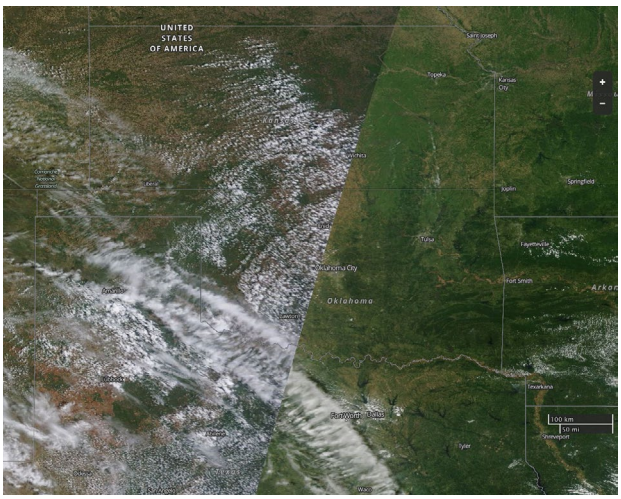

Figure 18. MODIS Terra corrected reflectance for 9-Jun-2015. Acquired from NASA EOSDIS Worldview, http://go.nasa.gov/1PpEM69.

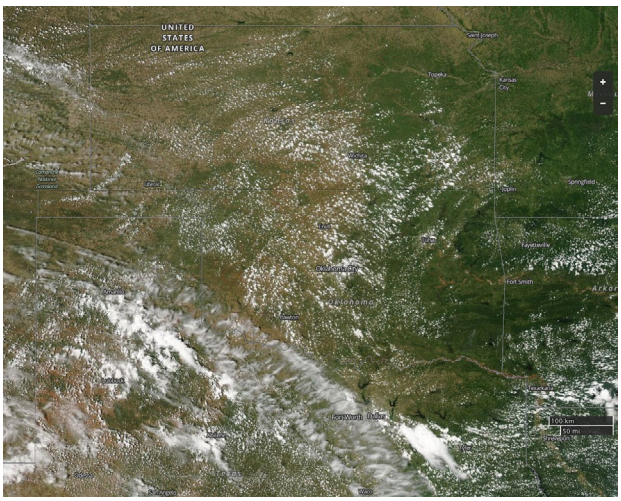

Figure 19. MODIS Aqua corrected reflectance for 9-Jun-2015. Acquired from NASA EOSDIS Worldview, http://go.nasa.gov/1OmdwL1.

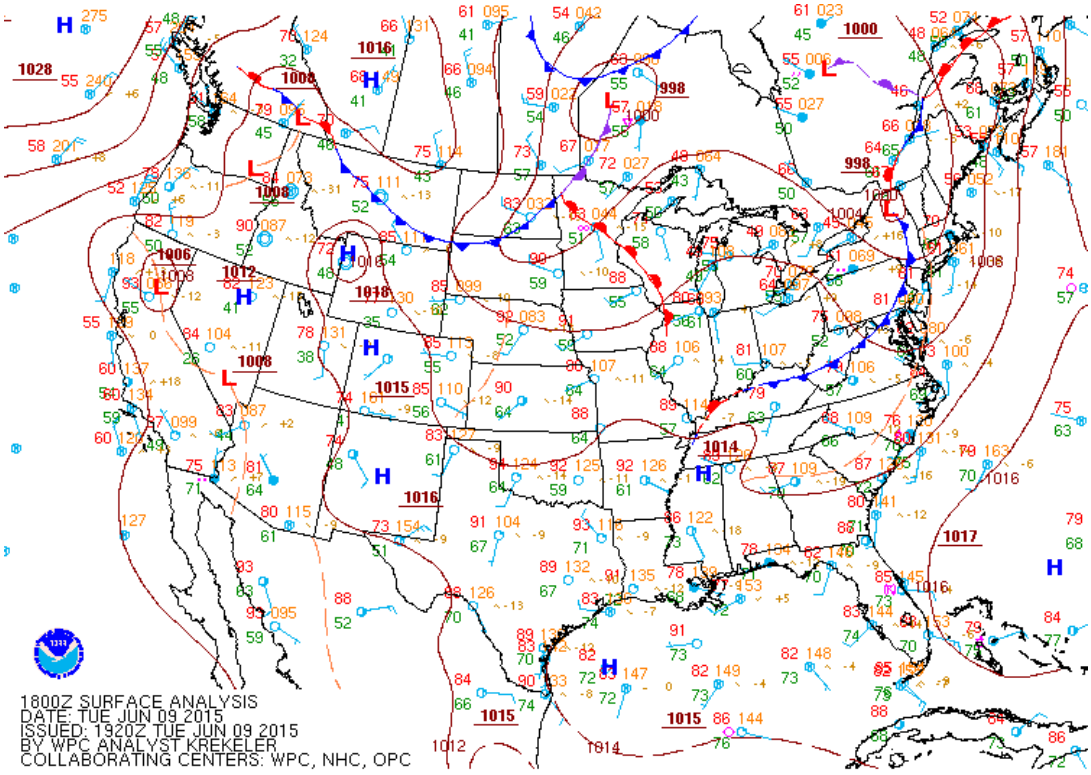

Figure 20. Surface analysis for 9-Jun-2015 18 UTC. Acquired from NWS Weather Prediction Center, http://www.wpc.ncep.noaa.gov/archives/web_pages/sfc/sfc_archive_maps.php?arcdate=06/09/2015&selmap=2015060918&maptype=namussfc.

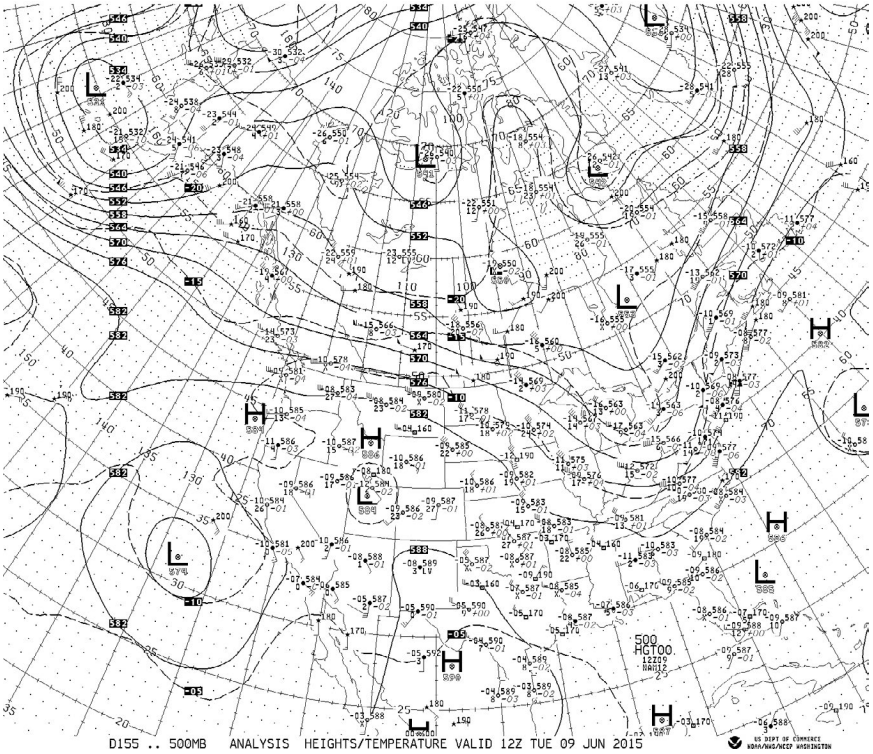

Figure 21. 500 hPa synoptic map for 9-Jun-2015 12 UTC. Acquired from Storm Research and Consulting, http://www.stormresearch.com/ncep/2015/2015_06/20150609122_500.tif.

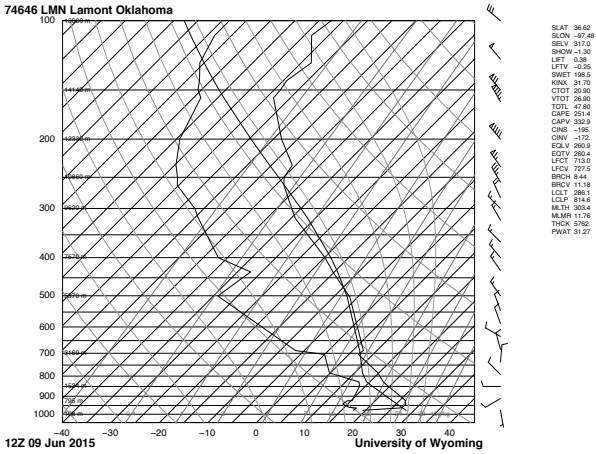

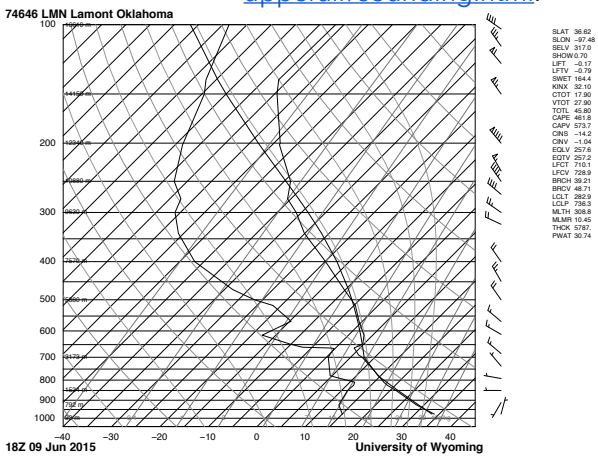

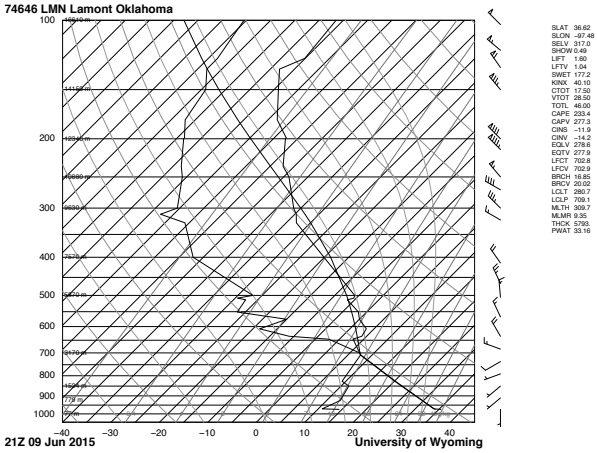

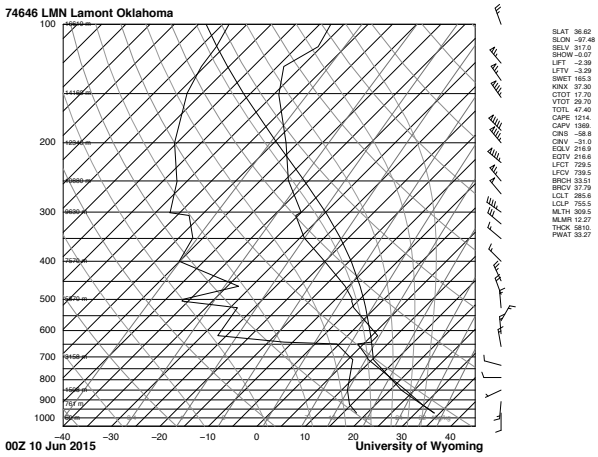

Figure 22. Skew-T log-P diagrams from Lamont, OK for 9-Jun-2015 at 12, 18, and 21 UTC and 10-Jun-2015 0 UTC. Acquired from U. Wyoming, http://weather.uwyo.edu/upperair/sounding.html.

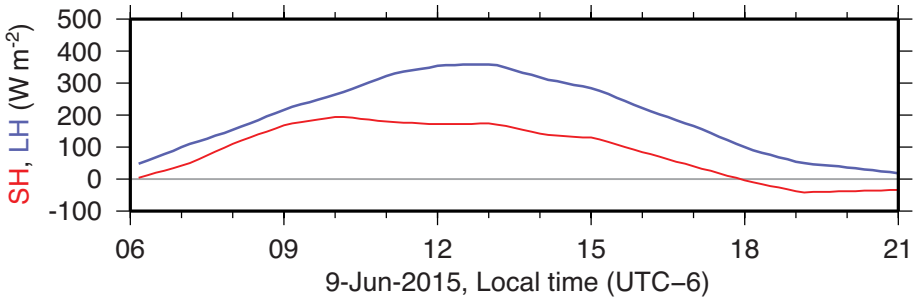

Figure 23. Surface sensible (red) and latent (blue) heat fluxes averaged for the SGP region by weighting fluxes based on percentage of land use type.

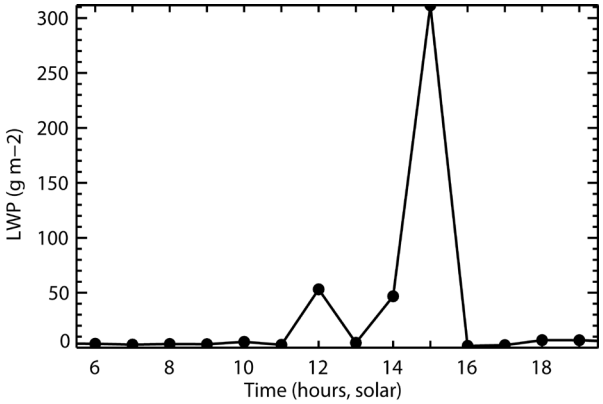

Figure 24. Cloud liquid water path for 9-Jun-2015 at the Central Facility based on MWRRet and AERIoe.

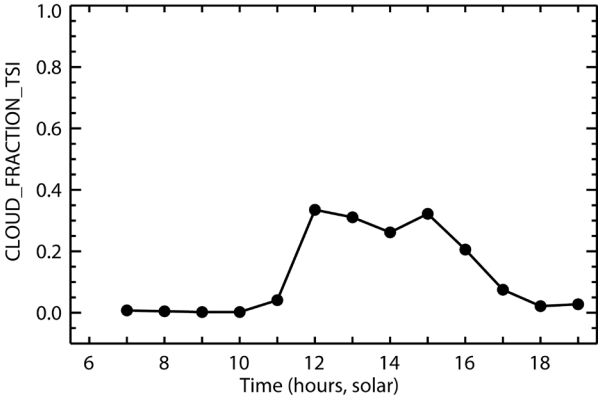

Figure 25. Cloud fraction derived from the TSI for 9-Jun-2015 at the Central Facility.

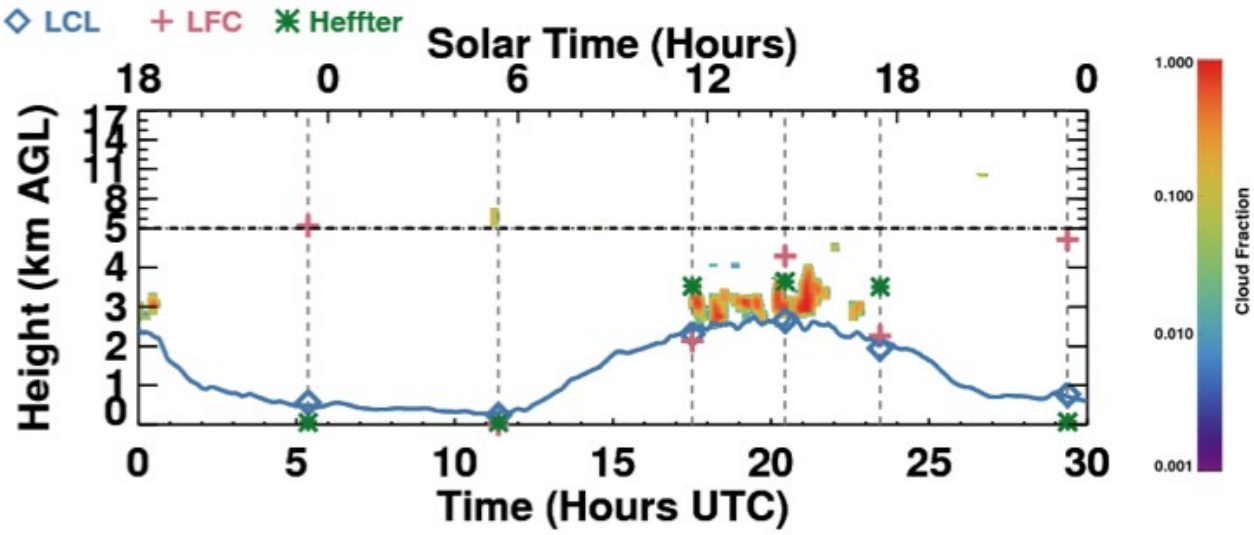

Figure 26. Cloud fraction profiles derived from the KAZR-ARSCL for 9-Jun-2015 at the Central Facility. Note the non-linear vertical axis that emphasizes the lower troposphere. Also indicated are the LCL, LFC, and PBL height based on the Heffter methodology, each of which are calculated from the SONDE product.

6.3 27-Jun-2015 Case

The overall synoptic situation on 27-Jun-2015 is defined by high pressure and a ridge over the western half of the CONUS and low pressure centered near the Great Lakes. At 12 UTC a stationary front extends from the center of this low to the southeast where it crosses the southeast corner of Oklahoma. This front moves southeastward during the day. The flow at the surface is from the northwest at 12 UTC and turns to easterly at 28-Jun 00 UTC. Upper level flow is northerly to northwesterly, and the shallow clouds generally flow north to south during the day. The morning sounding shows evidence of a residual layer at 12 UTC and both the moisture and temperature are well mixed by 18 UTC.

The morning has some cirrus advecting across the region that clear before the onset of shallow convection around 16 UTC. The TSI-based cloud fraction at the Central Facility is around 30–40% for most of the afternoon with hourly mean LWP varying from 20–110 g m^{-2}. It is clear from the GOES visible animation at http://iop.archive.arm.gov/arm-iop/0eval-data/gustafson/lasso-alpha1/docs/GOES_loops/GOES_vis_ict_20150627.gif that the air mass associated with the shallow convection is blown toward SGP from the north, with a leading edge of the shallow clouds visible in the animation along with banded structures advecting with the mean flow. These are more evident in the GOES animation than the Terra and Aqua images. It is possible that this mesoscale structure impacts the forcing generation, but overall, the region has somewhat uniform conditions within the forcing area.

Synoptic Conditions for 27-Jun-2015

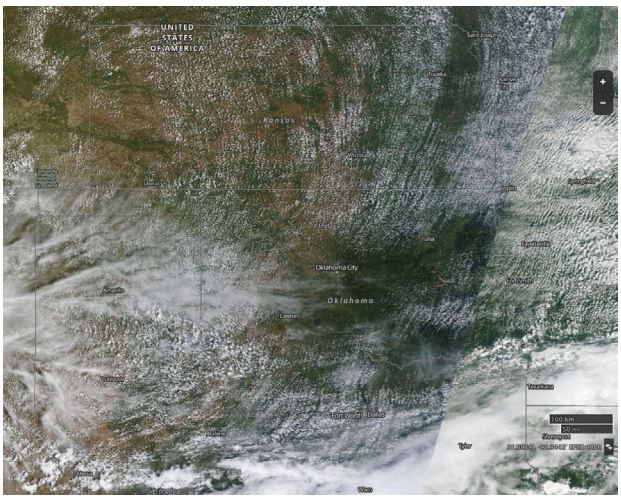

Figure 27. MODIS Terra corrected reflectance for 27-Jun-2015. Acquired from NASA EOSDIS Worldview, http://go.nasa.gov/1PpFqRd.

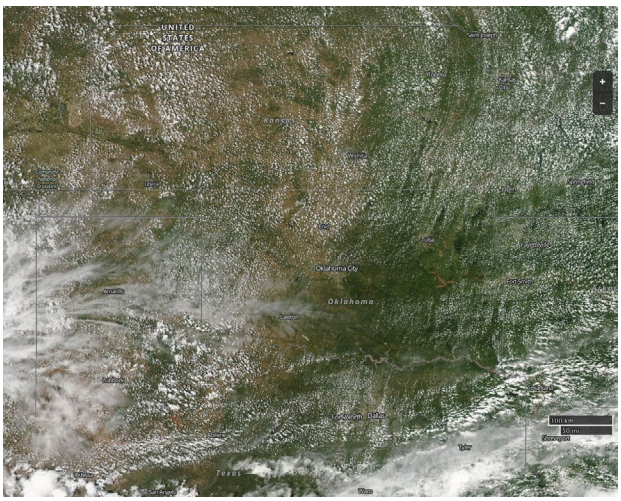

Figure 28. MODIS Aqua corrected reflectance for 27-Jun-2015. Acquired from NASA EOSDIS Worldview, http://go.nasa.gov/1PpFqAt.

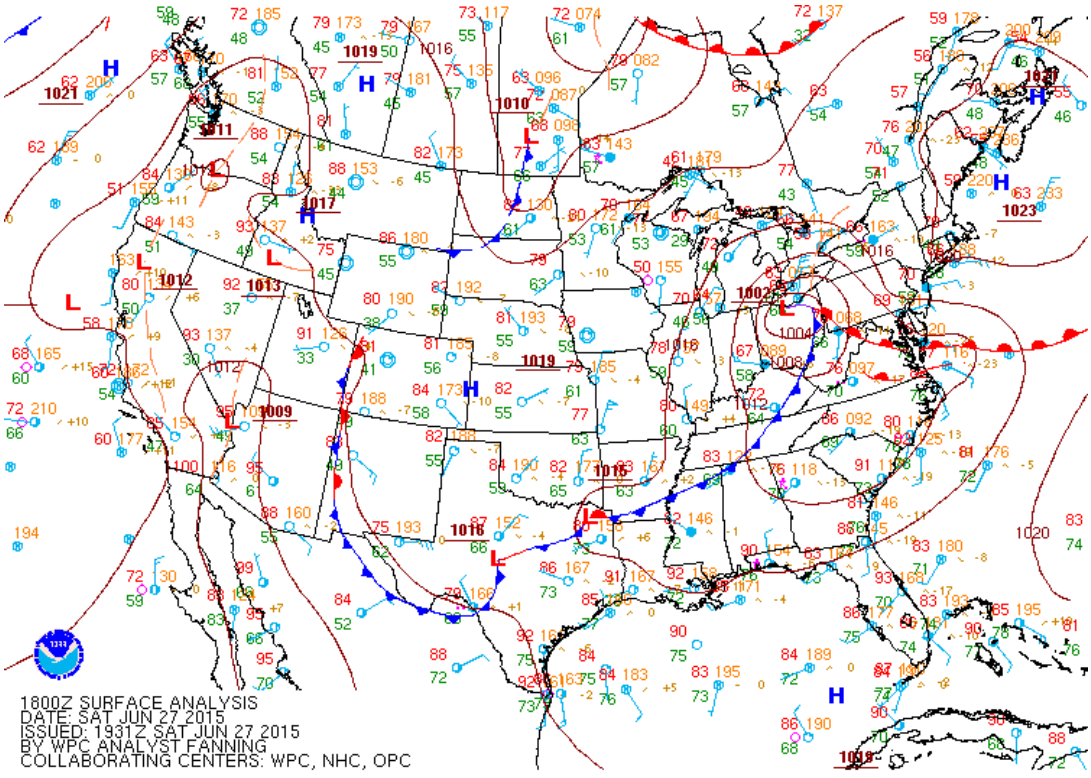

Figure 29. Surface analysis for 27-Jun-2015 18 UTC. Acquired from NWS Weather Prediction Center, http://www.wpc.ncep.noaa.gov/archives/web_pages/sfc/sfc_archive_maps.php?arcdate=06/27/2015&selmap=2015062718&maptype=namussfc.

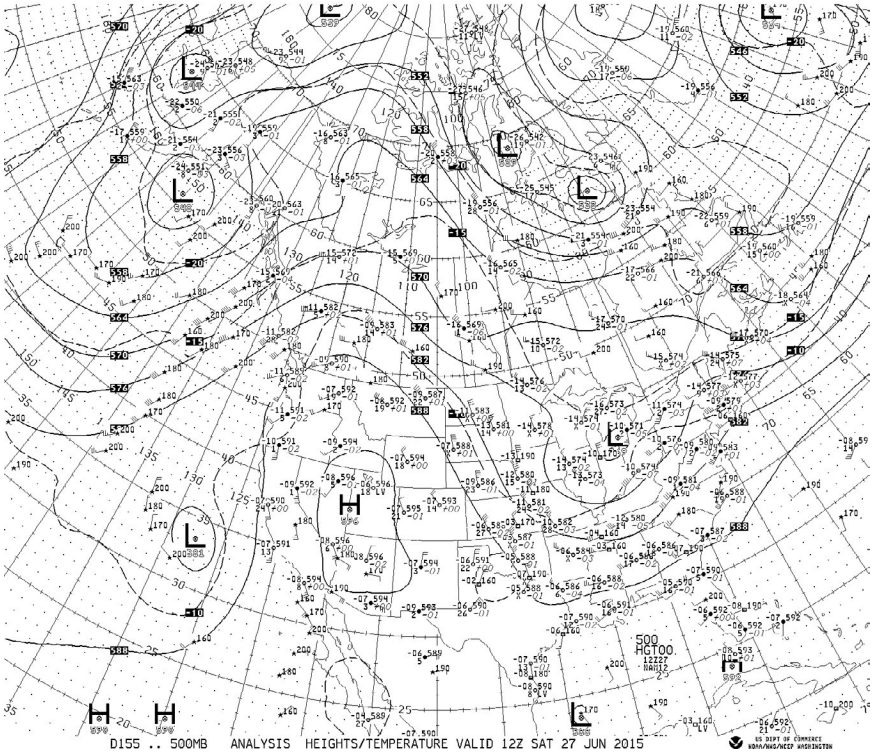

Figure 30. 500 hPa synoptic map for 9-Jun-2015 12 UTC. Acquired from Storm Research and Consulting, http://www.stormresearch.com/ncep/2015/2015_06/20150609122_500.tif.

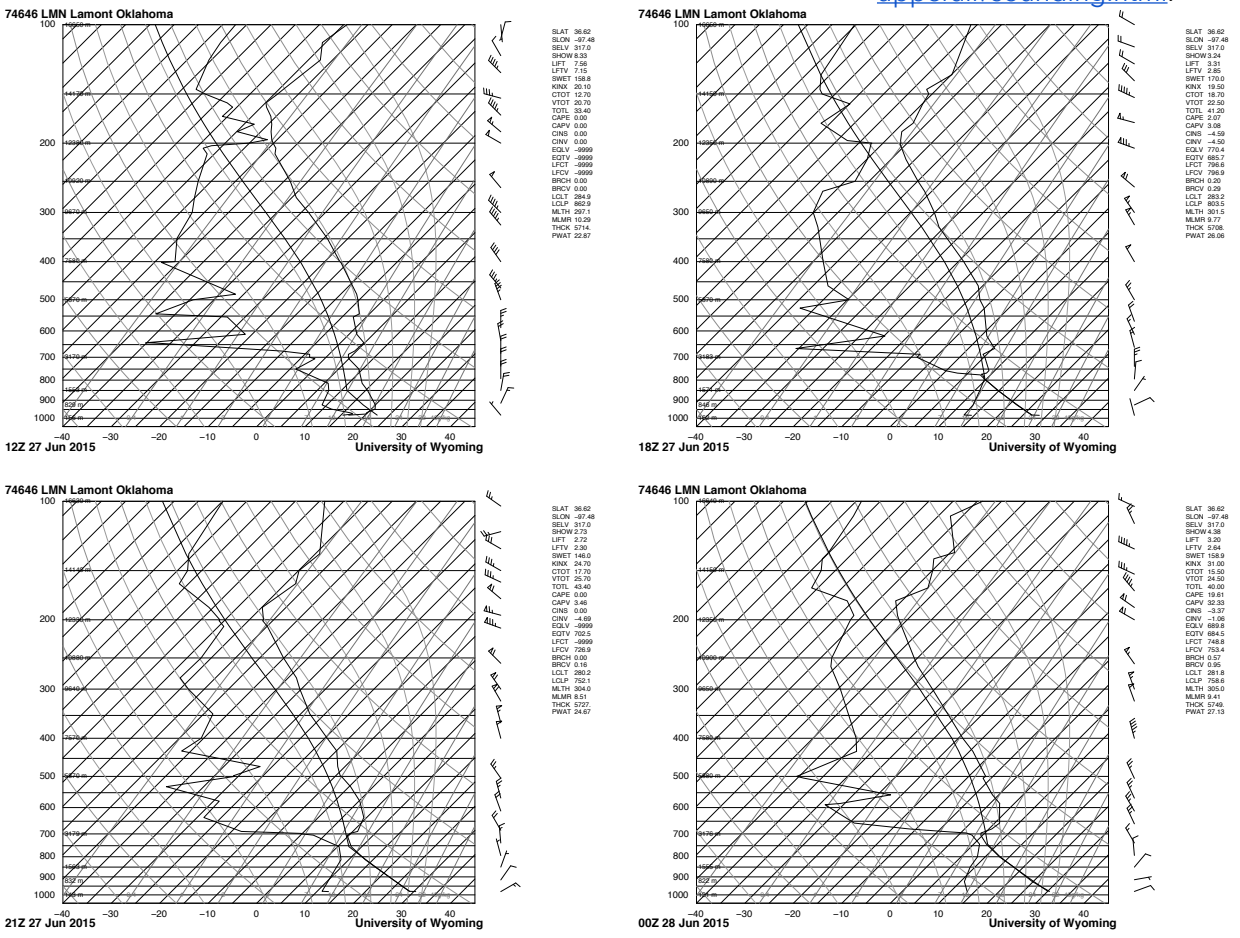

Figure 31. Skew-T log-P diagrams from Lamont, OK for 27-Jun-2015 at 12, 18, and 21 UTC and 28-Jun-2015 0 UTC. Acquired from U. Wyoming, http://weather.uwyo.edu/upperair/sounding.html.

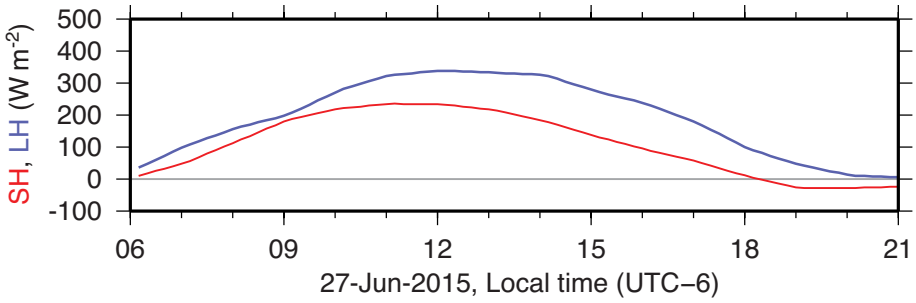

Figure 32. Surface sensible (red) and latent (blue) heat fluxes averaged for the SGP region by weighting fluxes based on percentage of land use type.

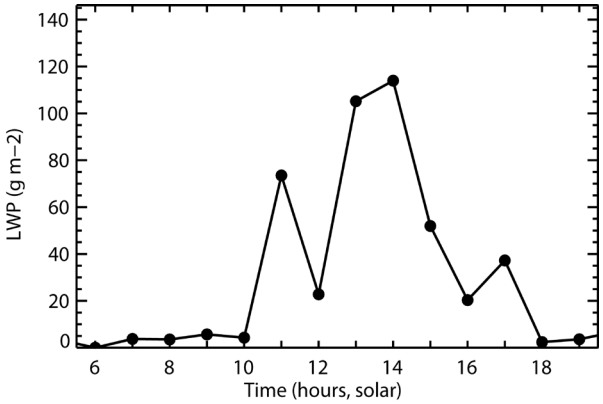

Figure 33. Cloud liquid water path for 27-Jun-2015 at the Central Facility based on MWRRet and AERIoe.

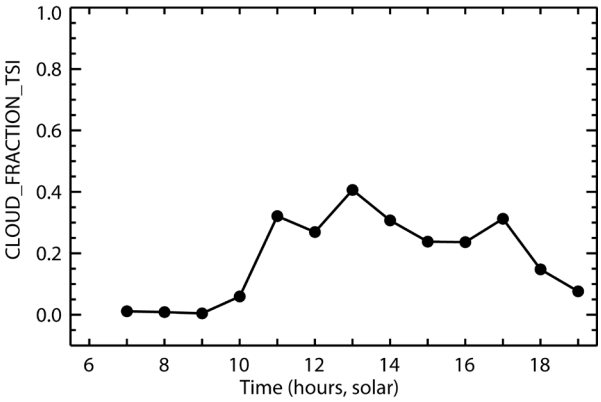

Figure 34. Cloud fraction derived from the TSI for 27-Jun-2015 at the Central Facility.

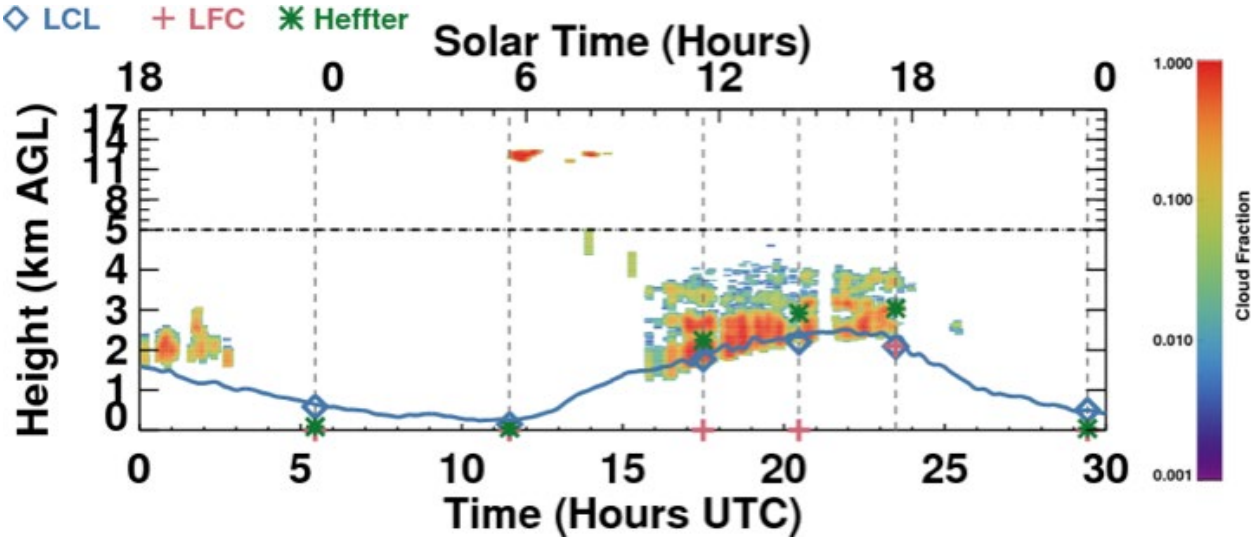

Figure 35. Cloud fraction profiles derived from the KAZR-ARSCL for 27-Jun-2015 at the Central Facility. Note the non-linear vertical axis that emphasizes the lower troposphere. Also indicated are the LCL, LFC, and PBL height based on the Heffter methodology, each of which are calculated from the SONDE product.

6.4 1-Aug-2015 Case

The synoptic situation on 1-Aug-2015 is shaped by a low pressure system over northeastern Canada, which has an associated trough impacting the eastern US. The western US is dominated by a large high pressure system, which encompasses the SGP. A large convective system passed over the entirety of Oklahoma on the previous day and deep convection is active in the Texas panhandle with associated clouds in Oklahoma at the beginning of 1-Aug. This is the source of much of the cirrus clouds observed at SGP throughout the day. Surface flow varies from west-southwesterly to east-southwesterly during the day with upper-level flow west-northwesterly. The soundings from the day show a developing boundary layer that has some structure within the PBL for moisture at 18 UTC and that is full mixed by 2-Aug 00 UTC. The soundings also show layering in the moisture, and to a lesser extent temperature, associated with varying wind directions.

Cirrus clouds are observed at SGP throughout most of the day and shallow clouds develop at 1730 UTC. The TSI-based cloud fraction exceeds 60% at 18 UTC and decreases after that with the 30–40% cloud fraction most of the afternoon. The LWP exceeds 180 g m^{-2} at 18 UTC and decreases after that time with fluctuating values. The GOES visible animation shows some of the shallow convection developing into deep convection west of SGP around 2230 UTC. The conditions triggering the deep convection plus the large cloud system in the Texas panhandle and southern Oklahoma imply heterogeneous conditions around SGP, which are averaged together to various degrees for the different sized forcing regions used for the LES.

Synoptic Conditions for 1-Aug-2015

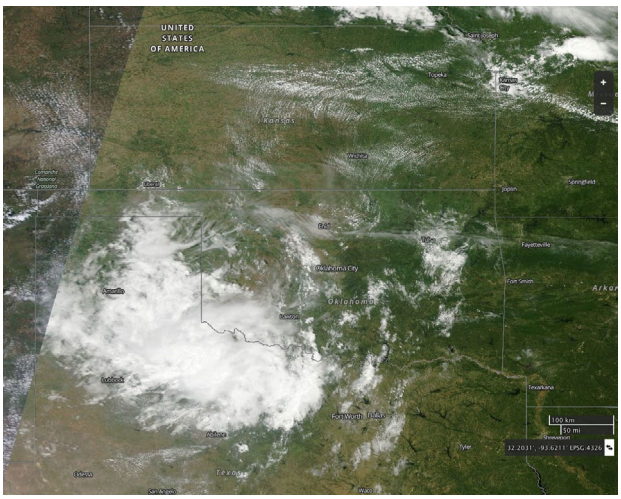

Figure 36. MODIS Terra corrected reflectance for 1-Aug-2015. Acquired from NASA EOSDIS Worldview, http://go.nasa.gov/1Omdnar.

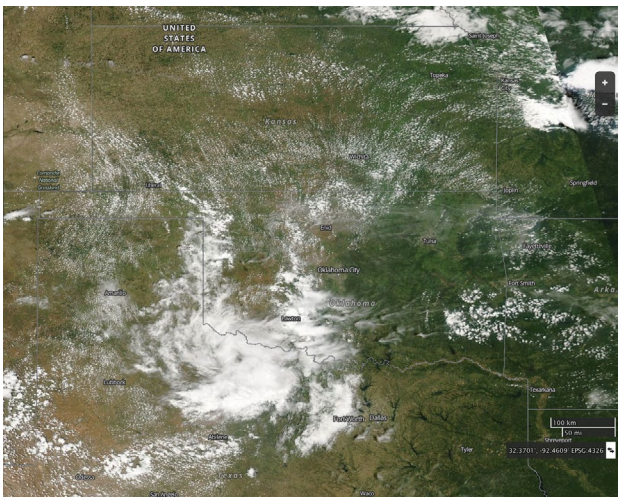

Figure 37. MODIS Aqua corrected reflectance for 1-Aug-2015. Acquired from NASA EOSDIS Worldview, http://go.nasa.gov/1PpFMHu.

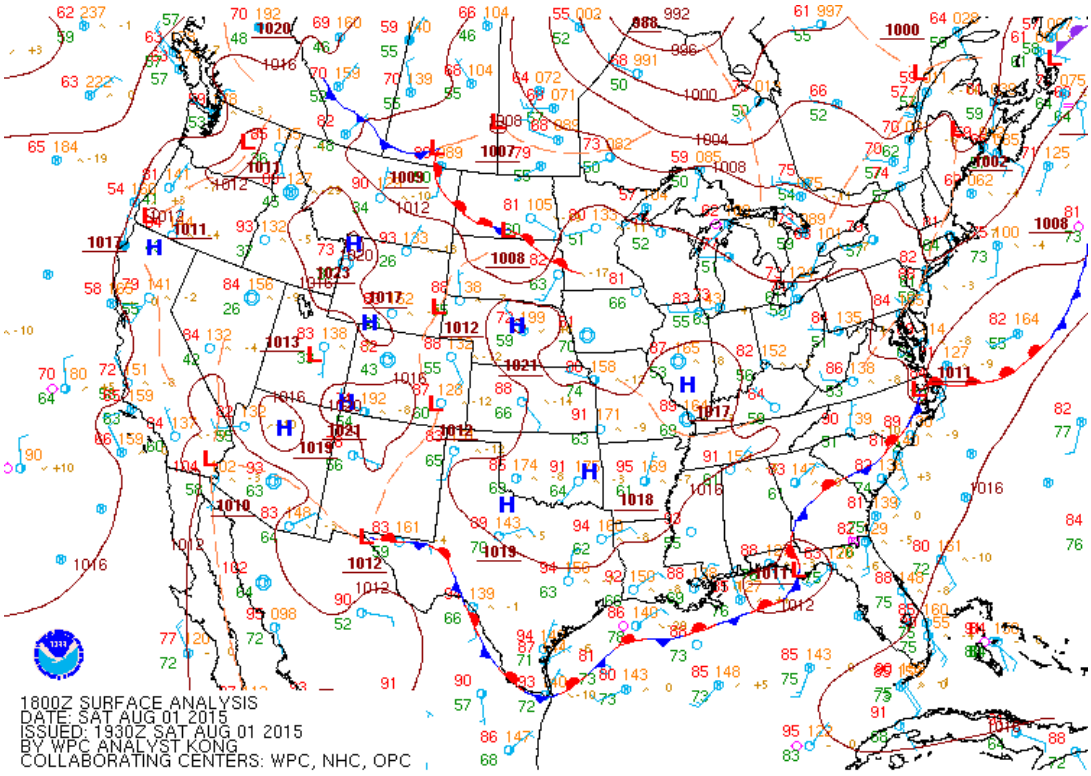

Figure 38. Surface analysis for 1-Aug-2015 18 UTC. Acquired from NWS Weather Prediction Center, http://www.wpc.ncep.noaa.gov/archives/web_pages/sfc/sfc_archive_maps.php?arcdate=08/01/2015&selmap=2015080118&maptype=namussfc.

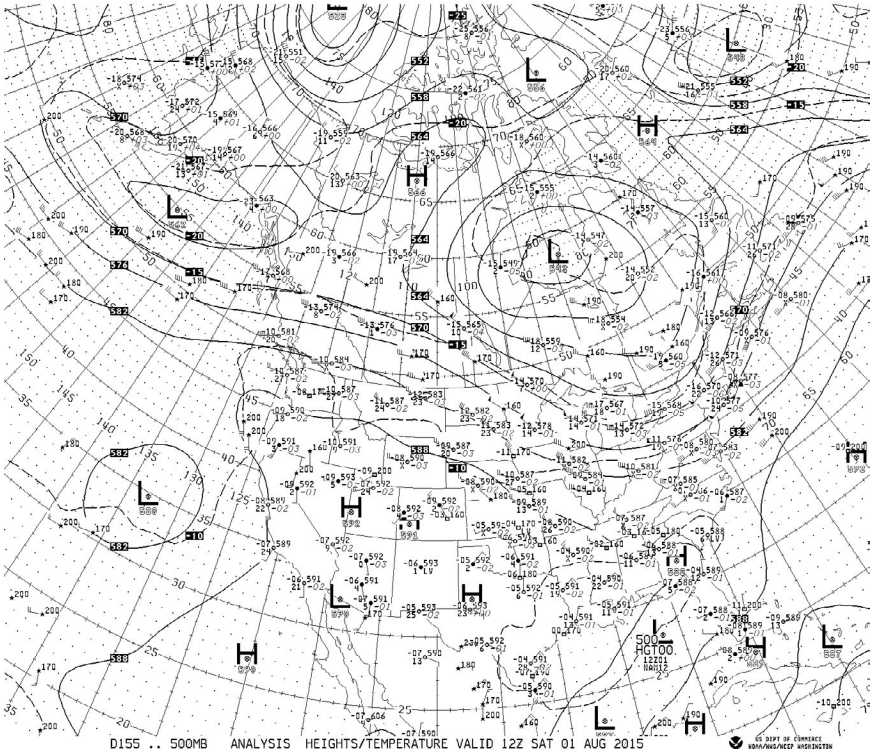

Figure 39. 500 hPa synoptic map for 9-Jun-2015 12 UTC. Acquired from Storm Research and Consulting, http://www.stormresearch.com/ncep/2015/2015_06/20150609122_500.tif.

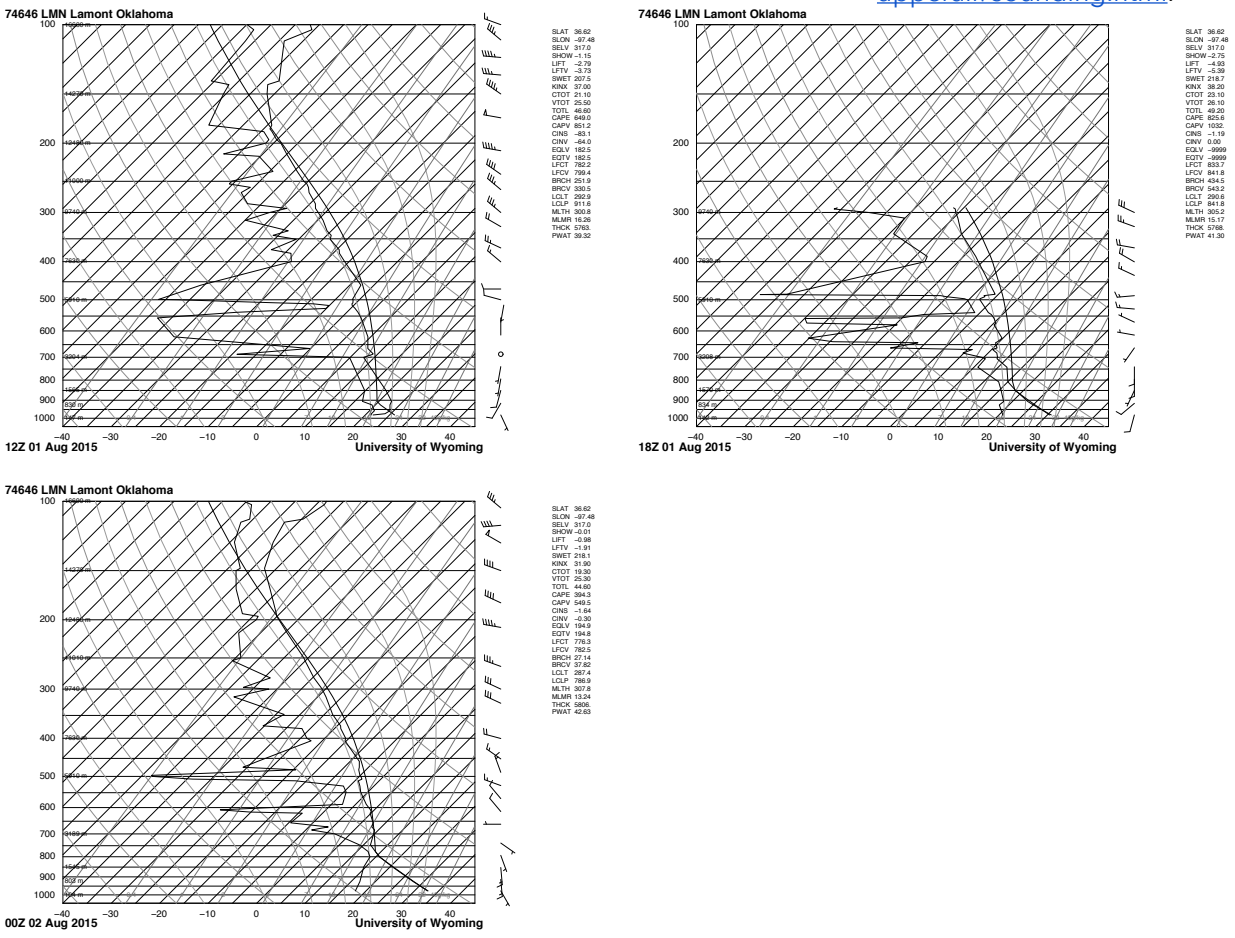

Figure 40. Skew-T log-P diagrams from Lamont, OK for 1-Aug-2015 at 12 and 18 UTC and 2-Aug-2015 0 UTC. Acquired from U. Wyoming, http://weather.uwyo.edu/upperair/sounding.html.

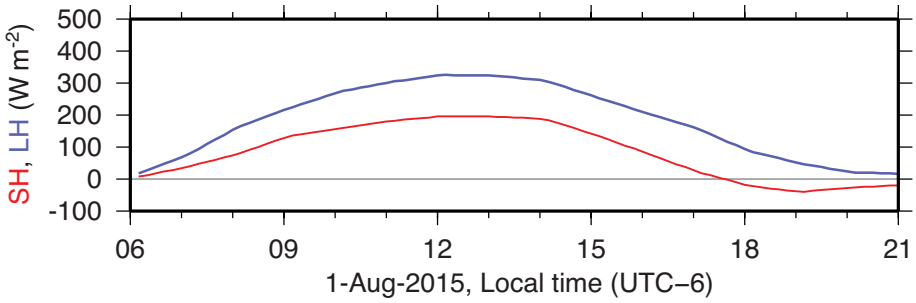

Figure 41. Surface sensible (red) and latent (blue) heat fluxes averaged for the SGP region by weighting fluxes based on percentage of land use type.

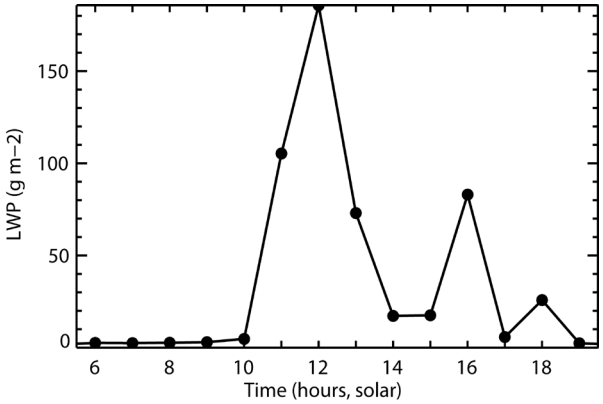

Figure 42. Cloud liquid water path for 1-Aug-2015 at the Central Facility based on MWRRet and AERIoe.

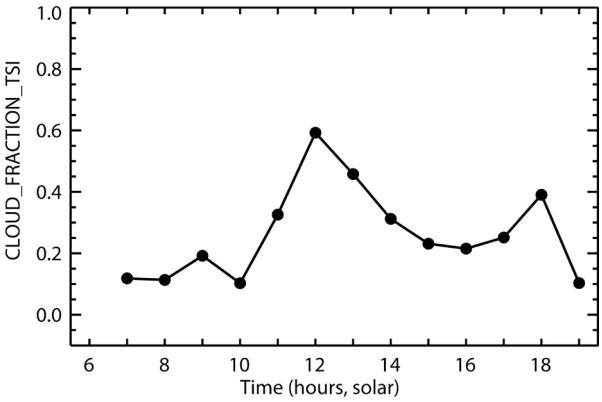

Figure 43. Cloud fraction derived from the TSI for 1-Aug-2015 at the Central Facility.

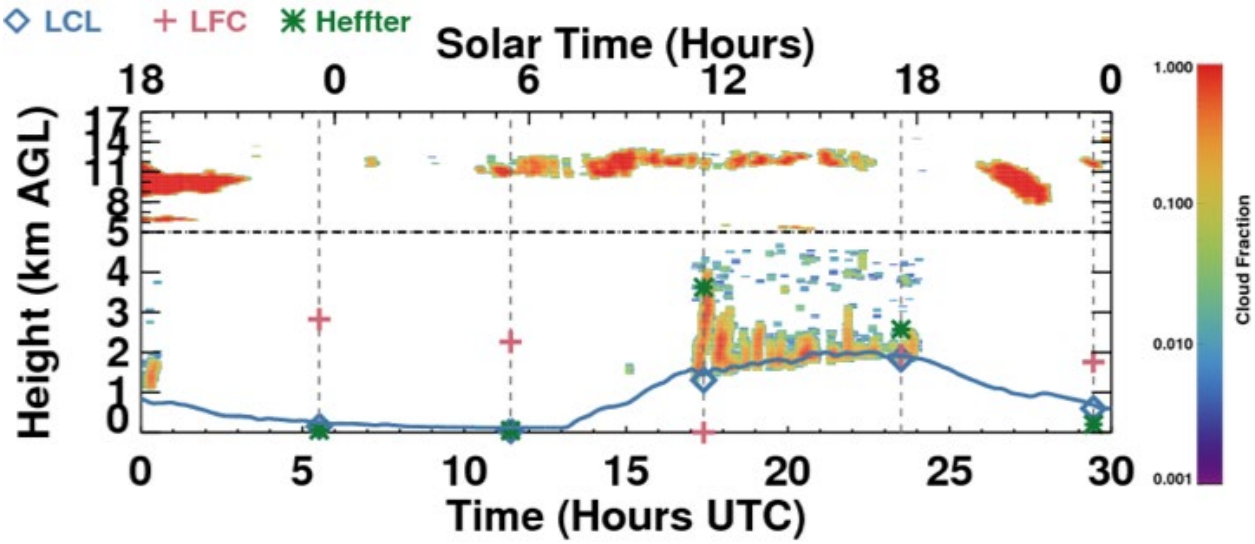

Figure 44. Cloud fraction profiles derived from the KAZR-ARSCL for 1-Aug-2015 at the Central Facility. Note the non-linear vertical axis that emphasizes the lower troposphere. Also indicated are the LCL, LFC, and PBL height based on the Heffter methodology, each of which are calculated from the SONDE product.

6.5 29-Aug-2015 Case

The 29-Aug-2015 case is strongly controlled by large-scale synoptic forcing. A cold front extends from a low over the Great Lakes and crosses Oklahoma to the east of SGP. The GOES visible animation at http://iop.archive.arm.gov/arm-iop/0eval-data/gustafson/lasso-alpha1/docs/GOES_loops/GOES_vis_ict_20150829.gif and the Terra and Aqua corrected reflectance images show that the shallow clouds observed at SGP are associated with the cold air behind the front and are at the southern tip of a larger cloudy region that consists of multi-layered clouds behind the front. Directly south of SGP the air is mostly clear until one gets farther south where the frontal clouds form along the cold front. A secondary low embedded within the cold front is also diagnosed along the southern Oklahoma border. Surface winds are generally northerly during the day with the winds above the boundary layer backing from westerly to northerly during the day. Winds in the upper troposphere are mostly westerly.

The clouds observed at the Central Facility are almost all shallow. They form around 1630 UTC and the cloud fraction increases for the next several hours, peaking around 65% at 19 UTC and decreasing again after that time. The hourly mean LWP during this cycle grows to about 26 g m^{-2}.

The large heterogeneity in the meteorology around SGP implies that both pre- and post-frontal air is mixed into the 300 km forcing region. Even the 75 km forcing region encompasses varying air masses since SGP lies on the southern tip of the shallow cloud region. Advection of the differing air masses also impacts the situation throughout the day, making it very difficult for the LES model.

Synoptic Conditions for 29-Aug-2015

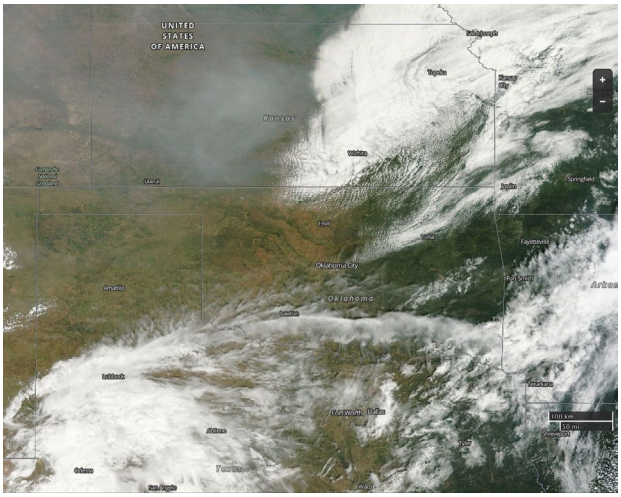

Figure 45. MODIS Terra corrected reflectance for 29-Aug-2015. Acquired from NASA EOSDIS Worldview, http://go.nasa.gov/1Omdu5G.

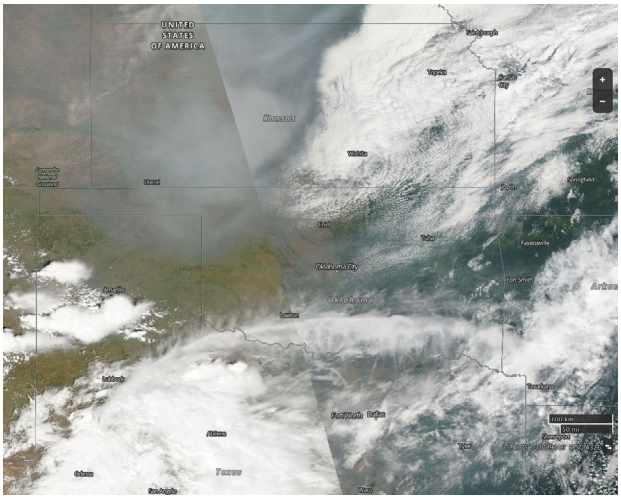

Figure 46. MODIS Aqua corrected reflectance for 29-Aug-2015. Acquired from NASA EOSDIS Worldview, http://go.nasa.gov/1PpGrZi.

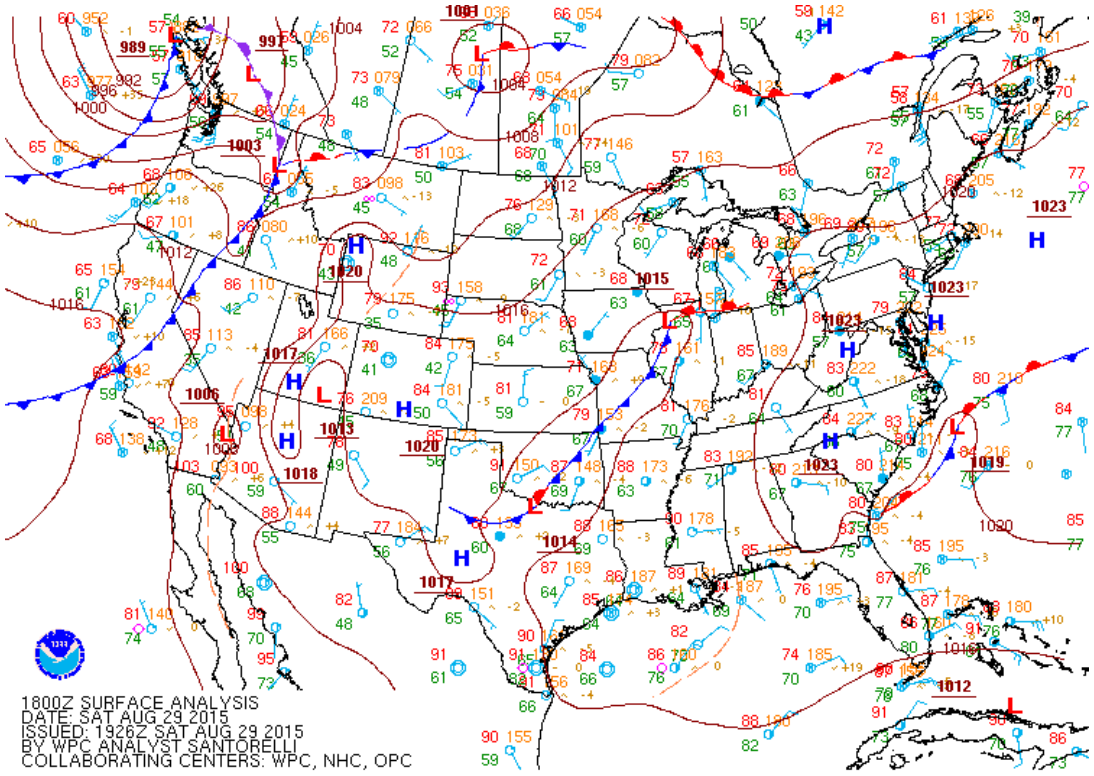

Figure 47. Surface analysis for 29-Aug-2015 18 UTC. Acquired from NWS Weather Prediction Center, http://www.wpc.ncep.noaa.gov/archives/web_pages/sfc/sfc_archive_maps.php?arcdate=08/29/2015&selmap=2015082918&maptype=namussfc.

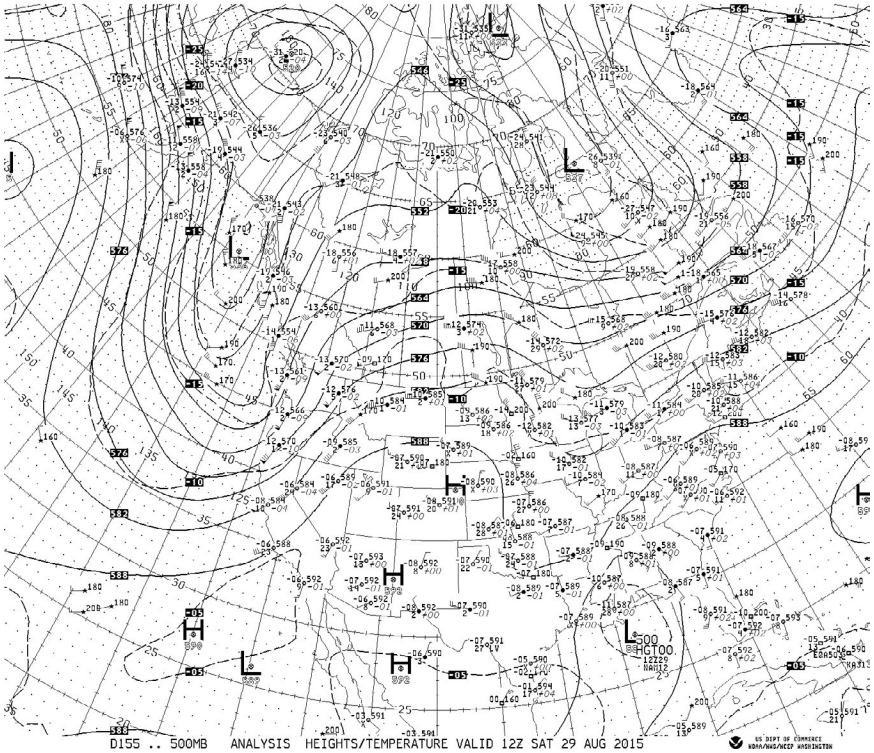

Figure 48. 500 hPa synoptic map for 9-Jun-2015 12 UTC. Acquired from Storm Research and Consulting, http://www.stormresearch.com/ncep/2015/2015_08/20150829122_500.tif.

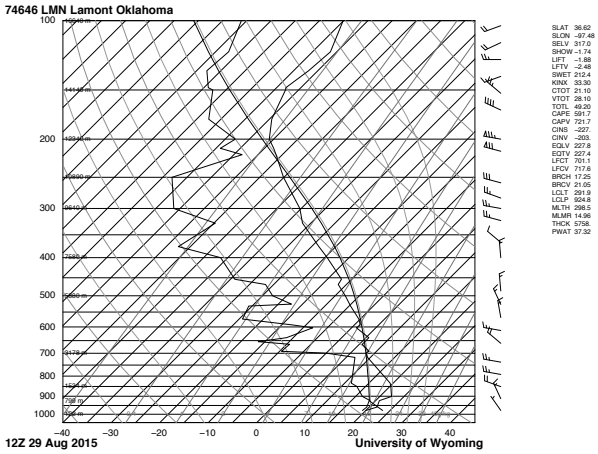

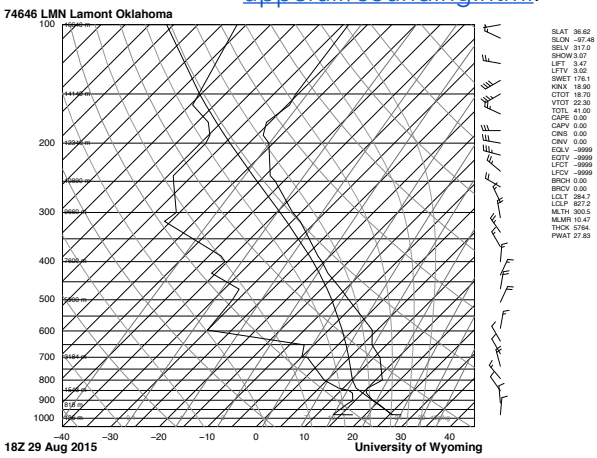

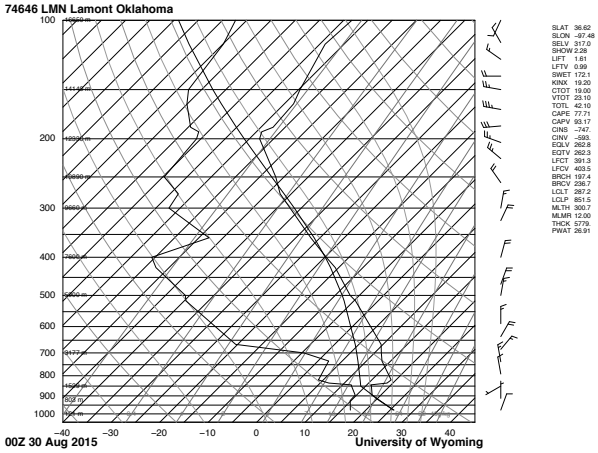

Figure 49. Skew-T log-P diagrams from Lamont, OK for 29-Aug-2015 at 12 and 18 UTC and 30-Aug-2015 0 UTC. Acquired from U. Wyoming, http://weather.uwyo.edu/upperair/sounding.html.

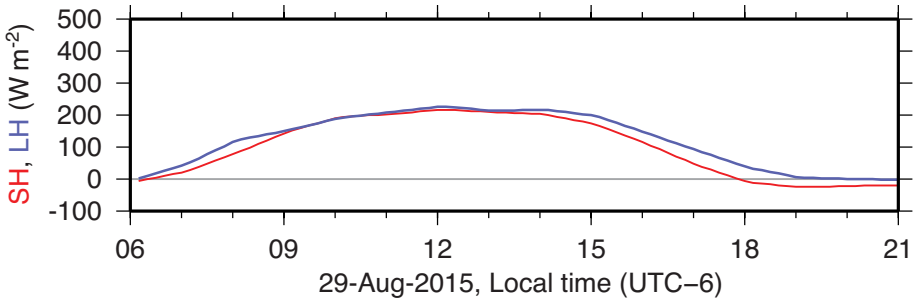

Figure 50. Surface sensible (red) and latent (blue) heat fluxes averaged for the SGP region by weighting fluxes based on percentage of land use type.

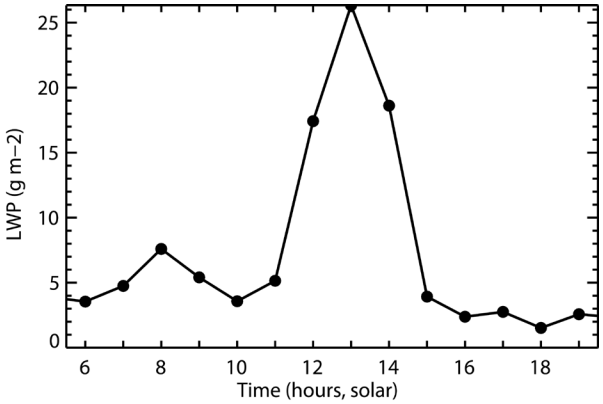

Figure 51. Cloud liquid water path for 29-Aug-2015 at the Central Facility based on MWRRet and AERIoe.

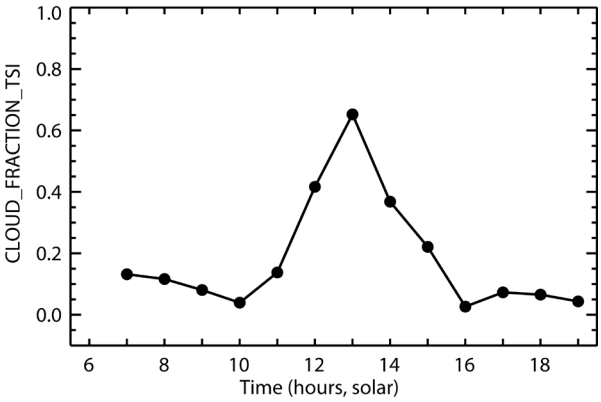

Figure 52. Cloud fraction derived from the TSI for 29-Aug-2015 at the Central Facility.

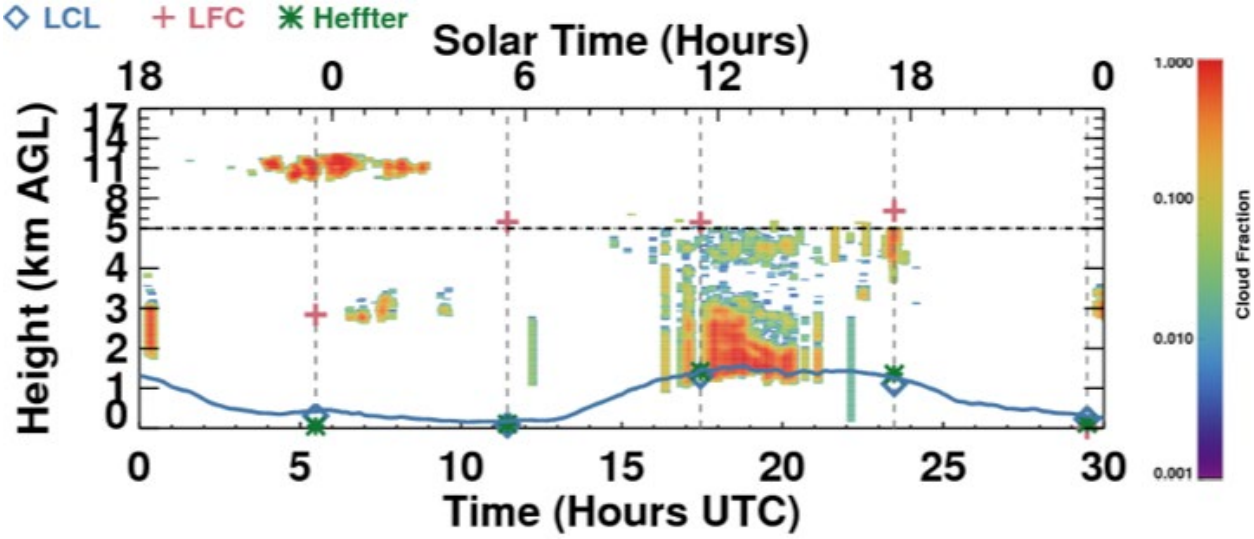

Figure 53. Cloud fraction profiles derived from the KAZR-ARSCL for 29-Aug-2015 at the Central Facility. Note the non-linear vertical axis that emphasizes the lower troposphere. Also indicated are the LCL, LFC, and PBL height based on the Heffter methodology, each of which are calculated from the SONDE product.

7 Acknowledgement

The LASSO Pilot Project team consists of William I. Gustafson Jr. (PI), Andrew M. Vogelmann (Co-PI), Xiaoping Cheng, Satoshi Endo, Zhijin Li, Tami Toto, and Heng Xiao. The LASSO Bundle Browser work is by Bhargavi Krishna. Funding provided by the U.S. Department of Energy Office of Science Biological and Environmental Research via the Atmospheric Radiation Measurement Climate Research Facility. We acknowledge the advice from external members for the LASSO Advisory Team: Maike Ahlgrimm (ECMWF), Chris Bretherton (University of Washington), Graham Feingold (NOAA ESRL), Chris Golaz (LLNL), David Turner (NOAA NSSL), Minghua Zhang (Stony Brook U.), and Jim Mather (ARM Technical Director). We acknowledge numerous members of the ARM infrastructure team for their coordination, installation, maintenance, processing, and advice given on the data products used and for LASSO product management. Portions of the work performed at 1) the Pacific Northwest National Laboratory (PNNL)—Battelle Memorial Institute operates PNNL under contract DEAC05-76RL01830, 2) Brookhaven National Laboratory, and 3) the Jet Propulsion Laboratory and the University of California Los Angeles via a subcontract through PNNL. Computation has been provided by 1) the Oak Ridge Leadership Computing Facility at the Oak Ridge National Laboratory, which is supported by the Office of Science of the U.S. Department of Energy under Contract No. DE-AC05-00OR22725; 2) the National Energy Research Scientific Computing Center, a DOE Office of Science User Facility supported by the Office of Science of the U.S. Department of Energy under Contract No. DE-AC02-05CH11231; and 3) PNNL Institutional Computing.

Appendix: Evaluation Data

In the Evaluation Data Section, the surface-based observations of in-cloud LWP, 1-D cloud fraction, and mid-boundary layer moisture and temperature were introduced that are described here in greater detail.

In-cloud liquid-water path (LWP)

LWP is derived from the 2-channel MWRRet microwave radiometer retrieval [Turner et al., 2007] and a new retrieval that use spectral infrared irradiances measured by the atmospheric emitted radiance interferometer (AERI) in a new optimal estimation framework (AERIoe) [Turner and Löhnert, 2014]. MWRRet uses measured microwave brightness temperatures (23.8 and 31.4 GHz) that have been bias corrected, yielding an LWP uncertainty of 20–30 g m^{-2} for a wide LWP dynamic range of 5 to 1000 g m^{-2}. AERIoe uses infrared radiances (8–13 μm) that provides sensitivity at small LWP (<~50 g m^{-2}), yielding an uncertainty of ~30% for LWP <5 g m^{-2} but manifests signal saturation by 50 g m^{-2}. A single, hybrid LWP dataset is formed by merging the AERIoe LWP values for <40 g m^{-2} and MWRRet values above that; thus, this product has the excellent AERIoe sensitivity at low LWP and the wide dynamic MWRRet range. Before merging these two datasets, the MWRRet values were regressed against the AERIoe LWP values to remove any systematic bias from the MWRRet values.

To obtain in-cloud LWP values, cloud screening was applied to the observations and simulations so that clear-sky values were not used in the time-averaged quantities. For observations, LWP values >1 g m^{-2} are screened as being cloudy values. In the simulations, the summation of the cloud and rainwater mixing ratios within a model grid cell is >1e–7 kg kg^{-1} to be considered 'cloud' and column integrals are computed of the cloudy cells to yield a 2-D LWP field. The average is taken of the LWP columns with values >1 g m^{-2} to produce the simulated in-cloud, domain-averaged LWP. In this procedure, the largest source of uncertainty is the incomplete sampling of broken clouds across the domain in the observations.

Currently, only LWP observations are available from the SGP central facility (single point). However, four new profiling boundary facilities have recently begun operation. When the LWP retrievals from these boundary sites become available in future releases, they will be used in a LWP average that will be more representative of the domain. Also, improvements to the AERIoe algorithm are planned so that it uses both the microwave and infrared radiances in a single LWP retrieval, thereby removing the need to merge the two separate LWP datasets.

1-D Cloud fraction (CF)

The TSI is a hemispheric-viewing camera providing retrievals of fractional sky cover during daytime for 'opaque' and 'thin' clouds. The opaque fractional value is used, which is most relevant to the boundary layer clouds of interest. Measurements from the 100° field-of-view are used to minimize CF overestimation due to scattering from cloud edges, particularly from clouds on the horizon. Cloud fraction is derived as 15 min averages that are averaged up to a 1 h value. Cloud fraction from ARSCL is derived as the cloud frequency per time interval as described in Xie et al. [2010], which assumes a horizontally uniform cloud field distribution (*i.e.*, the frozen turbulence assumption). Cloud fractions are 10 min averages of fractional occurrence computed from the vertically-resolved ARSCL cloud mask for clouds lower than 5 km, which are averaged up to a 1 h value. For ARSCL CF, the largest uncertainties are from the lack of using a radar simulator and from the application of the frozen turbulence assumption to broken cloud fields.

In simulations, cloud fraction is computed from the simulations in a manner that follows from the computation of in-cloud LWP: a grid cell is identified as cloudy if the sum of the cloud and rainwater mixing ratios is >1e–7 kg kg^{-1}, column integrals are taken of the cloudy cells to yield a 2-D LWP field, and cloud fraction is determined as the fraction of the 2-D grid with LWP >1 g m^{-2}, which is roughly the lower detectability limit of the measurements. Below this value, retrievals might measure haze or thin cirrus. The 1 g m^{-2} cutoff is somewhat arbitrary but yields similar cloud fractions to when 0.1 g m^{-2} is used. Note, however, that a 0 g m^{-2} cutoff can yield greater cloud fractions by up to 0.2 [Vogelmann et al., 2015].

Mid-Boundary layer moisture and temperature

A Raman lidar [Goldsmith et al., 1998] provides high frequency vertical profiles of the boundary layer Qv [Wulfmeyer et al., 2010], temperature [Newsom et al., 2013], and relative humidity (RH) computed from these measurements. The native temporal and vertical resolutions of the measurements are 10 s and 7.5 m, which are averaged and provided at 10 min and ~75 m resolution using automated processing algorithms [Turner et al., 2002; Newsom et al., 2013]. Measurements are valid above 300 m and below cloud base; below 300 m the Raman lidar retrievals are invalid due to receiver overlap considerations, and above cloud base the lidar signal saturates. The high spatial and temporal resolution of the Raman lidar data are valuable for assessing the simulated boundary layer evolution; however, note that it is a point measurement that cannot represent the total variation across the model-simulated domain.

References

Clothiaux, E. E., T. P. Ackerman, G. G. Mace, K. P. Moran, R. T. Marchand, M. A. Miller, and B. E. Martner (2000), Objective determination of cloud heights and radar reflectivities using a combination of active remote sensors at the ARM CART sites, *J. Appl. Meteorol.*, *39*(5), 645–665.

Clough, S. A., M. W. Shephard, E. Mlawer, J. S. Delamere, M. Iacono, K. Cady-Pereira, S. Boukabara, and P. D. Brown (2005), Atmospheric radiative transfer modeling: A summary of the AER codes, *J. Quant. Spectrosc. Radiat. Transfer*, *91*, 233–244, doi:10.1016/j.jqsrt.2004.05.058.

Deardorff, J. W. (1980), Stratocumulus-capped mixed layers derived from a three-dimensional model, *Boundary Layer Meteorol.*, *18*, 495–527, doi:10.1007/BF00119502.

Endo, S., A. M. Fridlind, W. Lin, A. M. Vogelmann, T. Toto, A. S. Ackerman, G. M. McFarquhar, R. C. Jackson, H. H. Jonsson, and Y. Liu (2015), RACORO continental boundary layer cloud investigations: 2. Large-eddy simulations of cumulus clouds and evaluation with in situ and ground-based observations, *J. Geophys. Res.*, *120*, 5993–6014, doi:10.1002/2014jd022525.

Goldsmith, J.E.M., F.H. Blair, S.E. Bisson, and D.D. Turner (1998) Turn-key Raman lidar for profiling atmospheric water vapor, clouds, and aerosols, *Appl. Opt.*, *37*, 4979–4990, doi:10.1364/AO.37.004979.

Heffter, J.L. (1980), Transport Layer Depth Calculations, *Second Joint Conference on Applications of Air Pollution Meteorology*, New Orleans, Louisiana.

Iacono, M. J., J. S. Delamere, E. J. Mlawer, M. W. Shephard, S. A. Clough, and W. D. Collins (2008), Radiative forcing by long-lived greenhouse gases: Calculations with the AER radiative transfer models, *J. Geophys. Res.*, *113*, D13103, doi:10.1029/2008jd009944.

Khairoutdinov, M. F., and D. A. Randall (2003), Cloud resolving modeling of the ARM summer 1997 IOP: Model formulation, results, uncertainties, and sensitivities, *J. Atmos. Sci.*, *60*, 607–625, doi:10.1175/1520-0469(2003)060<0607:Crmota>2.0.Co;2.

Lamer, K., and P. Kollias (2015), Observations of fair-weather cumuli over land: Dynamical factors controlling cloud size and cover, *Geophys. Res. Lett.*, *42*, 8693–8701, doi:10.1002/2015GL064534.

Li, Z., X. Cheng, W. I. Gustafson, and A. M. Vogelmann (2016), Spectral characteristics of background error covariance and multiscale data assimilation, *Int. J. Numer. Meth. Fluids*, in press, doi:10.1002/fld.4253.

Li, Z., S. Feng, Y. Liu, W. Lin, M. Zhang, T. Toto, A. M. Vogelmann, and S. Endo (2015a), Development of fine-resolution analyses and expanded large-scale forcing properties: 1. Methodology and evaluation, *J. Geophys. Res.*, *120*, 654–666, doi:10.1002/2014jd022245.

Li, Z. J., J. C. McWilliams, K. Ide, and J. D. Farrara (2015b), A multiscale variational data assimilation scheme: Formulation and illustration, *Mon. Wea. Rev.*, *143*, 3804–3822, doi:10.1175/mwr-d-14-00384.1.

Mlawer, E. J., S. J. Taubman, P. D. Brown, M. J. Iacono, and S. A. Clough (1997), Radiative transfer for inhomogeneous atmospheres: RRTM, a validated correlated-k model for the longwave, *J. Geophys. Res.*, *102*, 16663–16682, doi:10.1029/97jd00237.

Newsom, R.K., D.D. Turner, and J.E.M. Goldsmith (2013), Long-term evaluation of temperature profiles measured by an operational Raman lidar, *J. Atmos. Oceanic Technol.*, *30*, 1616–1634, doi:10.1175/JTECH-D-12-00138.1.

Mesinger, F., and T. L. Black (1992), On the impact on forecast accuracy of the step-mountain (eta) vs sigma coordinate, *Meteorol. Atmos. Phys.*, *50*, 47–60, doi:10.1007/bf01025504.

Morrison, H., J. Curry, and V. Khvorostyanov (2005), A new double-moment microphysics parameterization for application in cloud and climate models. Part I: Description, *J. Atmos. Sci.*, *62*, 1665–1677, doi:10.1175/JAS3446.1.

Morrison, H., G. Thompson, and V. Tatarskii (2009), Impact of cloud microphysics on the development of trailing stratiform precipitation in a simulated squall line: Comparison of one- and two-moment schemes, *Mon. Wea. Rev.*, *137*, 991–1007, doi:10.1175/2008MWR2556.1.

Skamarock, W. C., J. B. Klemp, J. Dudhia, D. O. Gill, D. M. Barker, M. G. Duda, W. Wang, and J. G. Powers (2008), A description of the advanced research WRF version 3, 113 pp, NCAR Technical Note, NCAR/TN-475+STR, National Center for Atmospheric Research, http://www.mmm.ucar.edu/wrf/users/docs/arw_v3.pdf.

Taylor, K.E. (2001), Summarizing multiple aspects of model performance in a single diagram, *J. Geophys. Res.*, *106*, 7183–7192.

Thompson, G., P. R. Field, R. M. Rasmussen, and W. D. Hall (2008), Explicit forecasts of winter precipitation using an improved bulk microphysics scheme. Part II: Implementation of a new snow parameterization, *Mon. Wea. Rev.*, *136*, 5095–5115, doi:10.1175/2008MWR2387.1.

Thompson, G., R. M. Rasmussen, and K. Manning (2004), Explicit forecasts of winter precipitation using an improved bulk microphysics scheme. Part I: Description and sensitivity analysis, *Mon. Wea. Rev.*, *132*, 519–542, doi:10.1175/1520-0493(2004)132<0519:EFOWPU>2.0.CO;2.

Turner, D.D., S.A. Clough, J.C. Liljegren, E.E. Clothiaux, K. Cady-Pereira, and K.L. Gaustad (2007), Retrieving liquid water path and precipitable water vapor from Atmospheric Radiation Measurement (ARM) microwave radiometers, IEEE Trans. *Geosci. Remote Sens.*, *45*, 3680–3690, doi:10.1109/TGRS.2007.903703.

Turner, D.D., R.A. Ferrare, L.A. Heilman Brasseur, W.F. Feltz, and T.P. Tooman (2002), Automated retrievals of water vapor and aerosol profiles from an operational Raman lidar, *J. Atmos. Oceanic Technol.*, *19*, 37–50, doi:10.1175/1520-0426(2002)019<0037:AROWVA>2.0.CO;2.

Turner, D.D., and U. Löhnert (2014), Information content and uncertainties in thermodynamic profiles and liquid cloud properties retrieved from the ground-based Atmospheric Emitted Radiance Interferometer (AERI). *J. Appl. Meteor. Clim.*, *53*, 752–771, doi:10.1175/JAMC-D-13-0126.1

Vogelmann, A.M., A.M. Fridlind, T. Toto, S. Endo, W. Lin, J. Wang, S. Feng, Y. Zhang, D. D. Turner, Y. Liu, Z. Li, S. Xie, A. S. Ackerman, M. Zhang, and M. Khairoutdinov (2015), RACORO Continental Boundary Layer Cloud Investigations. Part 1: Case Study Development and Ensemble Large-Scale Forcings, *J. Geophys. Res.*, *120*, doi:10.1002/2014JD022713.

Wulfmeyer, V., S. Pal, D.D. Turner, and E. Wagner (2010), Can water vapour Raman lidar resolve profiles of turbulent variables in the convective boundary layer? *Boundary Layer Meteor.*, *136*, 253–284, doi:10.1007/s10546-010-9494-z.

Xie, S. C., R. T. Cederwall, and M. H. Zhang (2004), Developing long-term single-column model/cloud system-resolving model forcing data using numerical weather prediction products constrained by surface and top of the atmosphere observations, *J. Geophys. Res.*, *109*, D01104, doi:10.1029/2003jd004045.

Xie, S., R. B. McCoy, S. A. Klein, R. T. Cederwall, W. J. Wiscombe, M. P. Jensen, K. L. Johnson, E. E. Clothiaux, K. L. Gaustad, C. N. Long, J. H. Mather, S. A. McFarlane, Y. Shi, J.-C.Golaz, Y. Lin, S. D. Hall, R. A. McCord, G.Palanisamy, and D. D. Turner (2010), CLOUDS AND MORE: ARM Climate Modeling Best Estimate Data, *Bull. Amer. Meteor. Soc.*, *91*, 13–20, doi:10.1175/2009BAMS2891.1.

Zhang, M. H., and J. L. Lin (1997), Constrained variational analysis of sounding data based on column-integrated budgets of mass, heat, moisture, and momentum: Approach and application to ARM measurements, *J. Atmos. Sci.*, *54*, 1503–1524, doi:10.1175/1520-0469(1997)054<1503:Cvaosd>2.0.Co;2.

Zhang, M. H., J. L. Lin, R. T. Cederwall, J. J. Yio, and S. C. Xie (2001), Objective analysis of ARM IOP data: Method and sensitivity, *Mon. Wea. Rev.*, *129*, 295–311, doi:10.1175/1520-0493(2001)129<0295:Oaoaid>2.0.Co;2.